NAZARBAYEV UNIVERSITY

Aeroacoustic Investigation of Propellers with Uneven Blade Spacing

by

Aruzhan Kantarbayeva

Submitted in partial fulfillment of the
requirements for the degree of Master of Science
in Mechanical and Aerospace Engineering

Date of Completion
May, 2025

Aeroacoustic Investigation of Propellers with Uneven Blade Spacing

by
Aruzhan Kantarbayeva

Submitted in fulfillment of the requirements for the degree of Master of Science in Mechanical and Aerospace Engineering

Nazarbayev University

May, 2025

Supervised by
Associate Professor Basman Elhadidi
Assistant Professor Altay Zhakatayev

Declaration

I, Aruzhan Kantarbayeva, declare that the research contained in this thesis, unless otherwise formally indicated within the text, is the author's original work. The thesis has not been previously submitted to this or any other university for a degree and does not incorporate any material already submitted for a degree.

Signature:

Date:

BLANK

Abstract

Propeller noise can be a significant health hazard affecting both mental and physical well-being. In recent years, the rapid growth of the Unmanned Aerial Vehicle (UAV) market has highlighted the importance of reducing noise generated by propellers. This thesis presents the investigation of aeroacoustic and aerodynamic performance of the rotors with uneven blade spacing as a potential noise mitigation technique.

APC 27×13 rotor was used to construct six rotor configurations with varying blade spacing. 4-bladed evenly spaced configuration served as the baseline rotor. Transient aerodynamic investigation were carried out using Unsteady Reynolds-Averaged Navier–Stokes (URANS) equations in an open-source computational fluid dynamics (CFD) solver. The rotation of the blades was achieved by using sliding mesh approach, which implements the physical rotation of the rotor. Pressure fields on the rotor blades obtained in the CFD simulation were interpolated onto a structured grid and subsequently used as an input data for an aeroacoustic model.

The acoustic modeling was conducted by integrating the Ffowcs Williams–Hawkings (FW–H) equation using the PSU-WOPWOP software. The results showed that the uneven blade spacing altered the periodicity of the acoustic pressure peaks, effectively redistributing tonal noise energy into lower frequency bands. Increasing the axial distance between the rotors led to a reduction of the loading acoustic pressure, which is attributed wake dissipation between the rotors.

To evaluate the advantages of using unsteady simulation, the results were compared to the steady-state Multiple Reference Frame (MRF) simulation. The unsteady simulations showed higher loading acoustic pressure. However, the contribution of loading noise to the total acoustic pressure remained limited. Furthermore, 5-bladed rotor configurations were examined to further assess the influence of index angle on the tonal noise behavior.

BLANK

Acknowledgments

First of all, I would like to express my sincere gratitude to Professor Basman Elhadidi. His guidance and support were essential during my studies at Nazarbayev University. I would also like to thank Professor Altay Zhakatayev, whose expertise and feedback were extremely helpful.

Finally, I would like to thank my family and friends. Their love and support encouraged me to embark on this journey.

Contents

Abstract **iii**

Acknowledgments **v**

List of Tables **ix**

List of Figures **xi**

Nomenclature **xiii**

1 Introduction **1**

1.1 Background 1
1.2 Research Hypothesis 3
1.3 Aims and Objectives 4
1.4 Outline 4

2 Literature Review **7**

2.1 Fundamentals of Sound and Its Measurement 7
2.2 Rotor Noise Generation 9
2.3 Lighthill's Acoustic Analogy 10
2.4 The Ffowcs Williams-Hawkings Equation 11
2.5 Stacked Rotors 12
2.6 Summary 15

3 Methodology **17**

3.1 Overview 17
3.2 CFD Simulations 19
3.3 Aeroacoustic Simulations 27

4 Results **31**

4.1 Aerodynamic Assessment 31
4.2 Acoustic Assessment 32
4.3 5-Bladed Configurations 40

5 Conclusions **43**

5.1 Summary 43

5.2 Recommendations for Future Work 44

Bibliography **45**

List of Tables

2.1 Summary of research studies on stacked rotors. 15

3.1 Configurations of the tested rotors. 18
3.2 OpenFoam grid sensitivity ($J = 0.3$). 24
3.3 PSU-WOPWOP grid sensitivity. 29

4.1 Thrust coefficient difference compared to the baseline rotor $\phi = 90°$, $\Delta x = 0D$. 31

List of Figures

1.1 eVTOL EH216-S developed by Ehang Intelligent [1]. 1
1.2 Joby S4, [2] 2
1.3 eVTOL market growth [3]. 2
1.4 Uneven blade spacing in NASA Puffin VTOL concept, [4] 3
1.5 Stacked rotor configuration: a) $\Delta\varphi$ - index angle, b) Δx - axial spacing 4

2.1 Equal loudness contours, [5] 8
2.2 A-weighting curve, adapted from [6] 8
2.3 Frequency spectra of the evenly spaced propeller. 9
2.4 Rotor noise sources, [7] 10
2.5 The definition of the moving surface, [8] 11
2.6 Apache AH-64 tail rotor 12
2.7 The experimental setup from [9] 14

3.1 APC 27×13 propeller, [10]. 17
3.2 Rotor geometry: a) rotor chord distribution; b) rotor twist distribution . 17
3.3 Methodology overview. 18
3.4 Case structure in OpenFOAM 19
3.5 Computational domain. 20
3.6 Geometry layout. 21
3.7 Mesh for a $\Delta\phi = 30°$, $\Delta x = 0.25D$ configuration 22
3.8 PIMPLE algorithm, [11]. 23
3.9 The change in thrust generated by the rotor over time at $J = 0.3$ 24
3.10 OpenFoam grid independence study. 25
3.11 Comparison of thrust coefficient with experimental data [12] and MRF simulation [13]. 26
3.12 Thrust coefficient comparison for a $\Delta\phi = 30°$, $\Delta x = 0D$ configuration 26
3.13 Surface mesh for a 2-bladed rotor. 28
3.14 Observer. 28
3.15 Case structure of the PSU-WOPWOP 29
3.16 Grid sensitivity study: a) 576 elements; b) 324; c) 144 30
3.17 Grid sensitivity study. 30

4.1 Q criterion isosurfaces: a) $\phi = 90°$, $\Delta x = 0D$; b) $\phi = 30°$, $\Delta x = 0D$; c) $\phi = 30°$, $\Delta x = 0.25D$; d) $\phi = 90°$, $\Delta x = 0.25D$ 32

4.2 Acoustic pressure comparison between the sliding mesh and MRF approaches for $\phi = 90°$, $\Delta x = 0D$. [13] 33
4.3 Total noise in the $\phi = 90°$, $\Delta x = 0D$ configuration. 34
4.4 Acoustic pressure comparison between the sliding mesh and MRF approaches for $\phi = 30°$, $\Delta x = 0D$. [13] 34
4.5 Acoustic pressure comparison at 90° and 30° index angles for 0D axial separation. 35
4.6 Total noise in the coplanar configurations. 36
4.7 Total acoustic pressure for the evenly spaced configuration at $\Delta x = 0$ and $\Delta x = 0.25D$. 36
4.8 Loading acoustic pressure comparison for $\phi = 90°$ and $\phi = 30°$ configurations. 37
4.9 Comparison of frequency spectra for $\phi = 90°$ and $\phi = 30°$ configurations. 38
4.10 Loading acoustic pressure comparison at 90° and 30° index angles. . . 38
4.11 Total acoustic pressure (a) and total noise (b) comparison at 90° and 30° index angles ($\Delta x = 0.25D$). 39
4.12 Total acoustic pressure (a) and total noise (b) comparison at 90° and 30° index angles ($\Delta x = 0.5D$). 39
4.13 5-Bladed configuration 40
4.14 Q-criterion, colored by the velocity. 40
4.15 Baseline 5-bladed configuration. 41
4.16 $\phi_{min} = 30°$, $\Delta x = 0.25D$ configuration. 41

Nomenclature

SPL	Sound Pressure Level
dB	Decibel
p	Mean pressure [Pa]
p_{ref}	Reference pressure (usually 20 μPa in air)
Hz	Hertz, unit of frequency
BPF	Blade Passing Frequency
RPS	Revolutions per second
BVI	Blade-Vortex Interaction
BWI	Blade-Wake Interaction
HSI	High-Speed Impulsive noise
ρ	Fluid density [kg/m^3]
ρ'	Density perturbation
p'	Acoustic pressure fluctuation [Pa]
ρ_0	Ambient (mean) density
p_0	Ambient (mean) pressure
υ_i	Component of velocity vector
σ_{ij}	Viscous stress tensor
δ_{ij}	Kronecker delta
f_i	Body force vector component
T_{ij}	Lighthill's tensor
FW-H	Ffowcs Williams-Hawkings equation
$\delta(f)$	Dirac delta function
$H(f)$	Heaviside function
UAM	Urban Air Mobility
UAV	Unmanned Aerial Vehicle
eVTOL	Electric Vertical Take-Off and Landing aircraft
uRANS	Unsteady Reynolds-Averaged Navier–Stokes
φ	Index angle (blade offset)
dBA	A-weighted decibels
D	Rotor diameter [m]
μ	Dynamic viscosity [Pa·s]
ν	Kinematic viscosity [$\nu = \mu/\rho$] [m^2/s]
u_i'	Fluctuating velocity component

$\overline{u_i' u_j'}$	Reynolds stress tensor components
k	Turbulence kinetic energy [m^2/s^2]
ω	Specific dissipation rate [1/s]
μ_t	Turbulent viscosity [Pa·s]
ε	Turbulence dissipation rate [$\omega k C_\mu$] [m^2/s^3]
I	Turbulence intensity
l	Turbulence length scale [m]
U	Inlet velocity [m/s]
T	Thrust force [N]
n	Rotor rotation speed [rev/s]
C_T	Thrust coefficient [$T/(n^2 D^4 \rho)$]
J	Advance ratio [$V_{inlet}/(nD)$]
Co	Courant number
δt	Time step [s]
δx	Characteristic cell size [m]
p_T'	Monopole (thickness noise) component of acoustic pressure [Pa]
p_L'	Dipole (loading noise) component of acoustic pressure [Pa]
υ_n	Surface-normal velocity component [m/s]
l_r, l_M	Components of loading vector in Farassat's formulation
M_r	Mach number component in observer direction
c_0	Speed of sound in the medium [m/s]
RPM	Rotations per minute
$\Delta\phi$	Index angle between rotor blades
Δx	Axial separation between rotors
p_{th}	Thickness acoustic pressure
p_l	Loading acoustic pressure
p_{tot}	Total acoustic pressure

Chapter 1

Introduction

1.1 Background

Aircraft noise is a significant environmental concern, that can be damaging to health. A study by Evans et al. [14] showed that children chronically exposed to aircraft noise demonstrate poor reading skills compared to their peers. Moreover, prolonged exposure to aircraft noise can disrupt sleep, which causes weak performance during the day and can lead to long-term health consequences.

The growing presence of small aircraft, particularly Unmanned Aerial Vehicles (UAVs) or drones, in urban areas has raised concerns about noise pollution. Although the noise levels from drones is significantly lower than traditional aircraft, constant exposure can negatively impact mood and overall well-being. The widespread use of UAVs may contribute to an uncomfortable and potentially harmful urban environment.

Aircraft noise also creates major challenges to the development of civil aviation and limits its applications. For example, eVTOL (electric Vertical Take-off and Landing) is a relatively new type of aircraft that has the potential to become a widespread mode of transportation in cities. Many companies are currently developing eVTOL technology, including Ehang Intelligent with its EH216-S (Figure 1.1). This two-passenger multicopter has been featured in flight demonstrations, showing the potential of urban air mobility. Another example is Joby Aviation S4 eVTOL (Figure 1.2), which was specifically designed for air taxi use[2].

Figure 1.1: eVTOL EH216-S developed by Ehang Intelligent [1].

Figure 1.2: Joby S4, [2]

eVTOL industry experienced intensive growth over the last years and is expected to continue expanding further [15]. However, the noise pollution remains a significant obstacle to their adoption. The eVTOL generated noise, particularly during takeoff and landing, can be disruptive in densely populated cities, making them unsuitable for urban environments where noise levels are already high. Addressing noise concerns is a crucial challenge for the successful introduction of eVTOLs into urban areas.

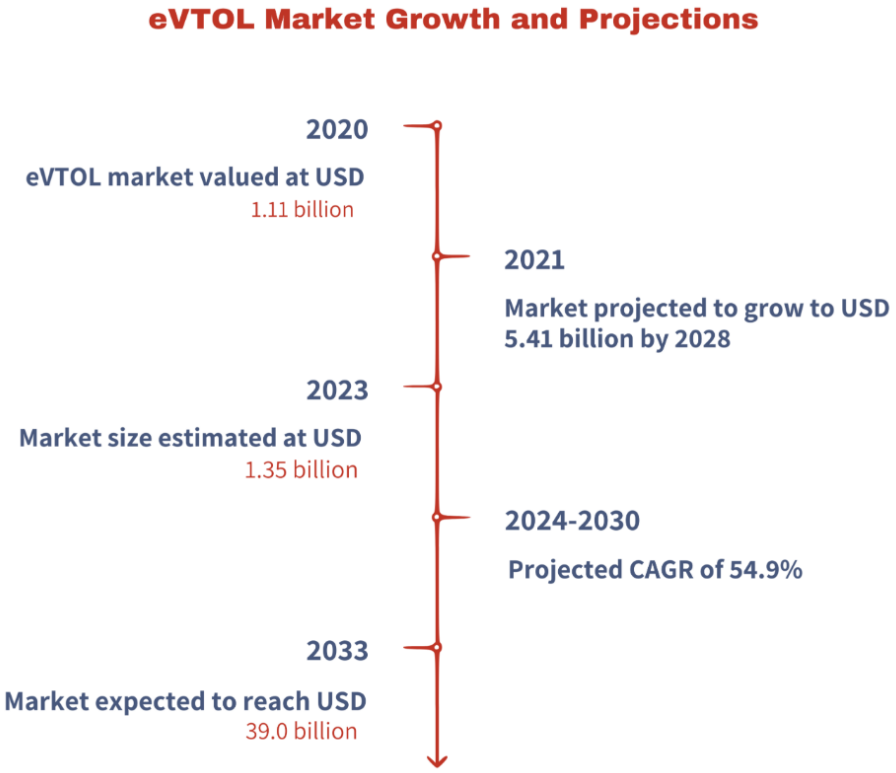

Figure 1.3: eVTOL market growth [3].

Over the years, various noise-reduction techniques were developed, most of which

involve geometric modifications to the propeller blades. However, the uneven blade spacing technique offers an alternative approach, that preserves the original blade structure and changes only the position of the blades. It was first introduced in the 1970 by Mellin et al. [16]. Since then, it was implemented in various application, including UAVs. One example is NASA's Puffin VTOL concept (Figure 1.4), which uses uneven blade spacing in its coaxial rotor configuration.

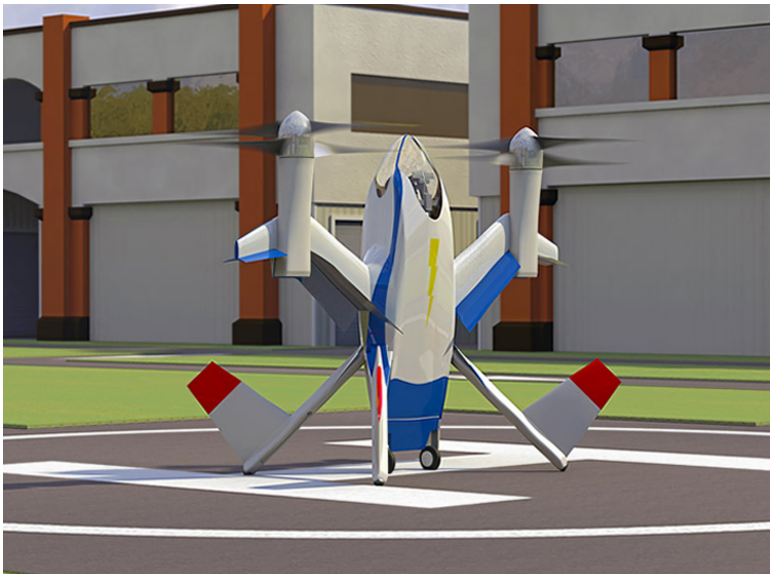

Figure 1.4: Uneven blade spacing in NASA Puffin VTOL concept, [4]

The potential applications of uneven blade spacing in modern aircraft still require further investigation. Understanding the impact of uneven blade spacing on noise reduction, aerodynamic performance, and structural integrity is essential for its integration into emerging aircraft technologies, such as eVTOLs. Further research is needed to investigate its effectiveness in noise reduction while maintaining efficiency, particularly in urban air mobility.

1.2 Research Hypothesis

Uneven blade spacing has been implemented in coaxial co-rotating rotors, or stacked rotors, as a way to reduce noise while maintaining aerodynamic performance. The noise reduction is possible due to the redistribution of noise energy using spacing modulation. The modal decomposition follows this relation:

$$m = nR \pm kV \tag{1.1}$$

where m is the modal wave number (with lower values corresponding to less noise), R - the number of blades in the front, V - number of blades in the back, n and k are integers.

When two rotors are positioned at different axial locations, each generates distinct noise signal that combine linearly. A typical stacked rotor configuration, including index angle and axial spacing, is shown in Figure 1.5.

Applying azimuthal modulation, i.e., varying the index angle, weakens the strength of dominant tonal modes and shifts the noise spectrum toward lower frequencies, resulting in a reduction in perceived noise levels. Additionally, introducing axial modulation by increasing the distance between the rotors allows for wake dissipation, resulting in reduced vortex interaction noise.

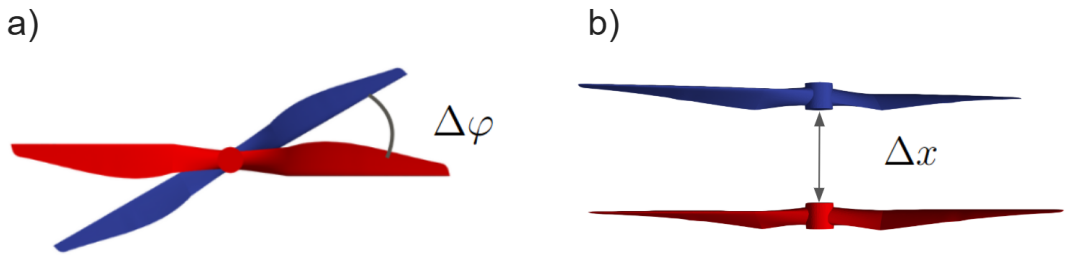

Figure 1.5: Stacked rotor configuration: a) $\Delta\varphi$ - index angle, b) Δx - axial spacing

1.3 Aims and Objectives

This thesis aims to investigate the aerodynamic and acoustic characteristics of propellers with uneven blade spacing using computational fluid dynamics (CFD) and aeroacoustic analysis. In order to reach this aim, the following objectives will be addressed:

1. Conduct CFD simulations of rotating propellers to analyze their aerodynamic performance.
2. Compute noise levels generated by the propellers using an aeroacoustic model.
3. Examine the impact of blade configuration on the noise characteristics.

1.4 Outline

The rest of the thesis is organized as follows:

Chapter 2 provides a literature review, covering the fundamentals of rotor noise generation, acoustic theory, and previous research.

Chapter 3 presents the methodology of the study for both aerodynamic and acoustic investigation.

Chapter 4 discusses the results obtained in the study.

Chapter 5 is the conclusions of the thesis along with suggestions for future work and possible improvements.

BLANK

Chapter 2

Literature Review

2.1 Fundamentals of Sound and Its Measurement

Sound is an acoustic wave propagating through the medium such as air or water, by causing pressure fluctuations in the medium. The pitch of the sound is determined by the frequency of the acoustic wave. The human ear can perceive sound waves within a frequency range of approximately 20 Hz to 20 kHz. Sound with a frequency above this upper limit is called ultrasound, while sound with a frequency below the lower limit is referred to as infrasound. However, different species have varying auditory ranges. For example, dogs can hear frequencies up to 45 kHz, while dolphins can detect sounds well beyond 100 kHz, which is necessary for echolocation.

The volume of the sound is characterized by the Sound Pressure Level (SPL), which is a ratio of the ambient pressure and the pressure in the region that was disturbed by an acoustic wave. SPL is measured in decibels (dB):

$$SPL = 20 \cdot log_{10}\left(\frac{p}{p_{ref}}\right) dB \tag{2.1}$$

The decibel scale is defined relative to a reference pressure level, typically 20 μPa in air, which corresponds to the threshold of human hearing. SPL is measured on a logarithmic scale to account fo the wide range of sound pressures the human ear can detect.

Auditory perception of loudness depends on the pitch or the frequency of the sound. Humans perceive sounds differently depending on the frequency. This effect was first discovered in an experimental study by Fletcher and Munson [17]. In this experiment, participants were asked to rate the loudness of sounds with varying pitches. The study revealed that humans are less sensitive to sounds with lower frequencies. Based on this data, Fletcher and Munson constructed equal-loudness contours (Fig 2.1), which illustrate the variation in SPL required for sounds to be perceived as equally loud across different frequencies.

Sound pressure level is often altered using frequency weightings to better reflect human perception of loudness. One such weighting is A-weighting, which reflects the 40 phon curve of the equal loudness contours. It amplifies the region from 1 to 6 kHz, while drastically cutting down the lower frequencies (Fig 2.2). The weighting is performed by adding A-weights to a sound level for each frequency band. This adjustment is particularly useful in the studies of environmental noise and its effects on

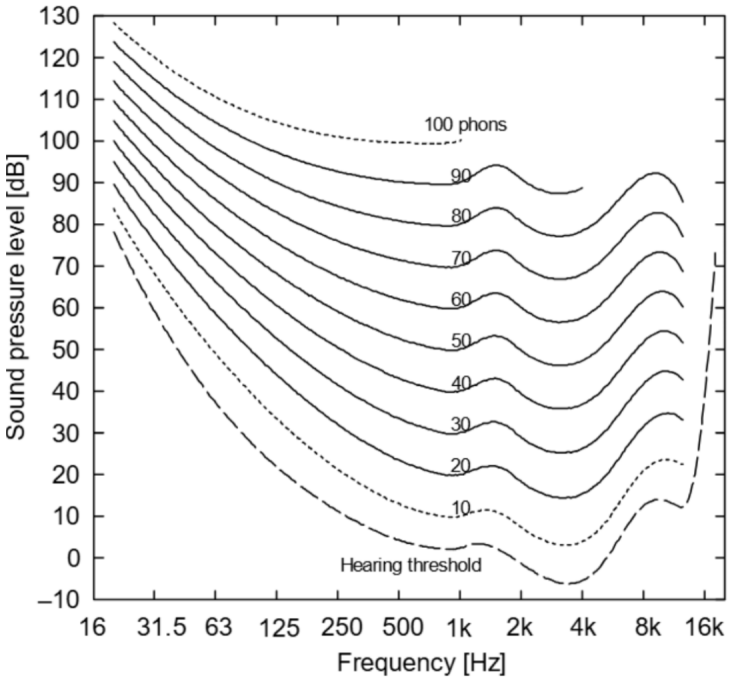

Figure 2.1: Equal loudness contours, [5]

human health and well-being. The A-weighted Sound Pressure Level is expressed in dBA.

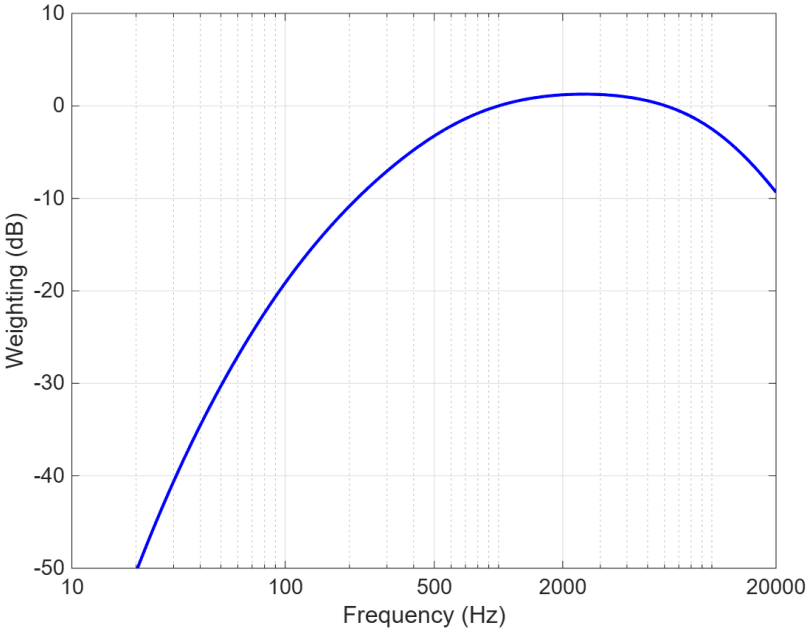

Figure 2.2: A-weighting curve, adapted from [6]

2.2 Rotor Noise Generation

The sound produced by the rotors can be divided into two categories based on the resulting frequency spectrum:

- Tonal noise: the spectrum of the tonal noise has distinct frequency components that produce clearly identifiable tones;
- Broadband noise: spreads across a wide range of frequencies without dominant tonal components;

Tonal noise is created by the periodic movement of the rotor blades. The frequency at which the blades of a rotor pass a stationary observer is called blade passing frequency (BPF). It can be calculated as the product of the rotational frequency of the rotor and the number of blades.

$$BPF = RPS \times Number\,of\,blades \tag{2.2}$$

BPF is the primary source of the tonal noise in operating rotors. The main tone occurs directly at BPF, but smaller frequency peaks are generated at the harmonic frequencies (2BPF, 3BPF, etc.) Figure 2.3 demonstrates the frequency spectrum foe the conventional 4-bladed propeller. The distinct noise peaks can be observed at the BPF frequency and its harmonics.

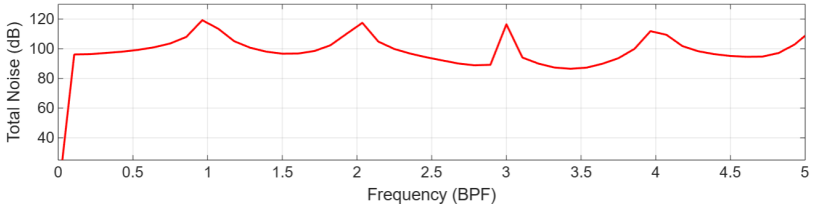

Figure 2.3: Frequency spectra of the evenly spaced propeller.

Broadband noise is caused by the interactions of the rotor with the turbulent flow. Broadband noise can significantly contribute to the overall sound level; however, it is generally less perceptible to the human ear than tonal noise.

Broadband and tonal noise in rotors can originate from various sources. The primary physical origins responsible for noise generation include:

- Thickness noise: generated by the displacement of the surrounding air due to the blade motion;
- Loading noise: generated by the aerodynamic forces acting on the rotating blades;
- High-speed impulsive (HSI) noise: occurs at high rotational speeds or elevated forward flight velocities;

Since thickness noise is caused by blade rotation, it produces distinct, identifiable tones at the blade passing frequency (BPF) and its harmonics. It is radiated within the plane of rotation, as shown in Figure 2.4 for a helicopter rotor. The main factors influencing thickness noise are rotational velocity and blade thickness.

HSI noise is generated under transonic flow conditions due to the formation of shock waves. It radiates in the same direction as thickness noise.

Loading noise is generated by the force exerted by the blade on the surrounding fluid and can be either steady or unsteady. The loading noise generated by steady aerodynamic forces propagates below the plane of rotation. Unsteady loading emerges when the flow is changed rapidly due to the blade's interaction with the surrounding fluid. Instances of unsteady loading include blade-vortex interaction (BVI) and blade-wake interaction (BWI).

Blade-vortex interaction is a specific subset of unsteady loading caused by the interaction between tip vortices and the blade. The noise produced by BVI is directed downward, out of the plane of rotation.

Blade-wake interaction can be a significant source of noise in systems with multiple rotors, such as coaxial co-rotating and contra-rotating configurations.

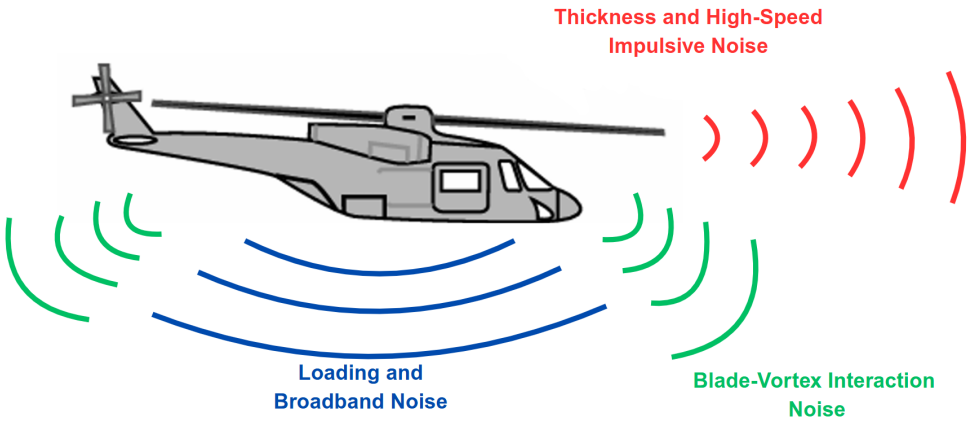

Figure 2.4: Rotor noise sources, [7]

2.3 Lighthill's Acoustic Analogy

Determining the acoustic field by directly solving the compressible Navier-Stokes equations is challenging due to their nonlinearity. Additionally, the sound generated by the flow accounts for only a small fraction of the total flow energy. To address these challenges, in 1952 Lighthill proposed an acoustic analogy that models the turbulent flow as an acoustic source that radiates sound to the far field [18]. He reformulated mass and momentum conservation equations into an inhomogeneous wave equation,

describing pressure or density perturbations as the source of sound generation. Equation (2.3) is known as Lighthill's analogy.

$$\frac{1}{c^2}\frac{\partial^2 p'}{\partial t^2} - \frac{\partial^2 p'}{\partial x_i^2} = \frac{\partial^2}{\partial x_i \partial x_j}(\rho v_i v_j - \sigma_{ij}) - \frac{\partial f_i}{\partial x_i} + \frac{\partial^2}{\partial t^2}(\frac{p'}{c^2} - \rho') \tag{2.3}$$

where c is the speed of sound in the medium under consideration, $p' = p - p_0$, $\rho' = \rho - \rho_0$.

Equation (2.3) can be rewritten for ρ' by subtracting $c^2 \frac{\partial^2 \rho'}{\partial x_i^2}$:

$$\frac{\partial^2 \rho'}{\partial t^2} - c^2 \frac{\partial^2 \rho'}{\partial x_i^2} = \frac{\partial^2 T_{ij}}{\partial x_i \partial x_j} - \frac{\partial f_i}{\partial x_i} \tag{2.4}$$

where T_{ij} - Lighthill's tensor:

$$T_{ij} = \mathcal{P}_{ij} + \rho v_i v_j - c^2 \rho \delta_{ij} \tag{2.5}$$

The terms of the Lighthill's tensor can be evaluated using turbulence models.

2.4 The Ffowcs Williams-Hawkings Equation

Lighthill's analogy, while powerful, did not account for presence of solid boundaries in the flow. In 1969, Ffowcs Williams and Hawkings extended Lighthill's analogy to include sound generation from moving surfaces [19]. This formulation is used in many noise predicting tools, including PSU-WOPWOP.

Figure 2.5 illustrates the moving surface, which acts as a sound source in Ffowcs Williams-Hawkings formulation. The volume $B(t)$, which is enclosed by the surface $S(t)$, is described by the function $f(\boldsymbol{x}, t)$ (equation (2.6)).

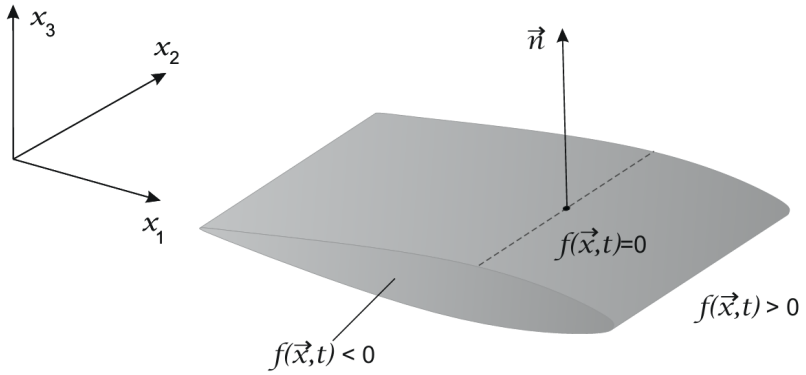

Figure 2.5: The definition of the moving surface, [8]

$$\left.\begin{array}{ll} f(\boldsymbol{x},t) < 0 & if\ \boldsymbol{x} \in B(t) \\ f(\boldsymbol{x},t) = 0 & if\ \boldsymbol{x} \in S(t) \\ f(\boldsymbol{x},t) > 0 & outside\ B(t) \end{array}\right\} \tag{2.6}$$

The FW-H equation is given by:

$$\frac{1}{c^2}\frac{\partial^2 p'}{\partial t^2} - \nabla^2 p' = \frac{\partial}{\partial t}[\rho v_n \delta(f)] - \frac{\partial}{\partial x_i}[p_{ij} n_j \delta(f)] + \frac{\partial^2}{\partial x_i \partial x_j}[H(f) T_{ij}] \tag{2.7}$$

Where $\delta(f)$ is the Dirac delta function, $H(f)$ - Heaviside function. Since surface $S(t)$ is impermeable, its normal velocity must be equal to the normal velocity of the fluid: $u_n = v_n = -\frac{\partial f}{\partial t} = -\left(\frac{\partial f}{\partial x_i}\right)\left(\frac{\partial x_i}{\partial t}\right)$.

The three terms on the right-hand side of equation (2.7) correspond to three sound sources, commonly referred to as monopole, dipole and quadrupole. The monopole and dipole terms are typically the most significant, as they mostly contribute to tonal noise. The quadrupole term accounts for the broadband noise generated by wake and turbulence interactions. However, the computation of the volume integral is computationally expensive. For this reason, the quadrupole term is often ignored in many aeroacoustic solvers.

2.5 Stacked Rotors

Propellers with uneven blade spacing have been a subject of investigation for several decades. The tail rotor of Apache AH-64 helicopter (Fig 2.6) is a stacked rotor with $55°$ angle separation which was initially designed as a way to improve mechanical clearance, but was later found to reduce noise emissions.

Figure 2.6: Apache AH-64 tail rotor

In the early 1990s Dobrzynski proposed stacked rotors with uneven blade spacing as a way to reduce noise emissions [20]. A noise reduction of 4 dBA was observed when the blade spacing angle was varied between 15° and 40° degrees. Also, the stacked rotor configuration enables adjustment of the blade spacing angle while maintaining balance. Dobrzynski found no reduction in aerodynamic performance in stacked rotors compared to coplanar ones.

Stacked rotors with uneven blade spacing have attracted a lot of attention in recent years due to the development of urban air mobility (UAM). The use of unmanned aerial vehicles (UAV) and electric vertical take-off and landing (eVTOL) aircraft in urban areas requires a significant reduction in noise emissions that stacked rotors might be able to address. An experimental study by Tinney and Valdez showed the effect of axial distance between rotors, separation angle and rotational speed on the thrust and aeroacoustic properties of the stacked propellers in hover conditions [21]. The separation angle seemed to have the most effect on the thrust. However, the separation angle for the maximum thrust coefficient was more sensitive to axial distance at lower rotational speeds. Tinney and Valdez demonstrated that a noise reduction of 15 dB(A) can be achieved by adjusting the index angle, axial distance and rotational speed, while maintaining thrust.

Whiteside et al. conducted numerical and experimental research of the 3×3 stacked rotors with various stacking distances and index angles [22]. The aeroacoustic and aerodynamic performance of stacked rotors was compared to a baseline 6-bladed coplanar rotor. Unlike the experimental results in [21], the best aerodynamic performance was recorded for the stacked rotor with symmetrical blade spacing. It was found that the simultaneous increase of the axial distance and the decrease of the index angle increases the low frequency tonal noise and produces oscillations in the higher frequency broadband noise. However, all stacked rotor configurations produced smaller broadband noise levels compared to a baseline rotor. Whiteside et al. argue that the reduction of the broadband noise levels is due to the downwash of the upper rotor which reduces the angle of attack on the lower rotor. The same effect was observed by Hong et al. in the numerical study of stacked rotors in hover [23]. The inflow of the upper rotor is intensified by the lower rotor sucking in the upper rotor's wake. Consequently, the aerodynamic performance is diminished due to the decrease of the effective angle of attack. All stacked rotor configurations in this study showed poor aerodynamic performance when compared to a 2-bladed coplanar rotor. However, Platzer et al. observed a thrust increase in stacked rotors with unevenly spaced blades [24]. The experimental and numerical study was performed on the 4-bladed stacked and counter-rotation propellers. The CFD study was carried out using the unsteady Reynolds-averaged Navier–Stokes (uRANS) model. The maximum total thrust was generated at the index angle $\varphi = +22.5$. Also, the influence of the index

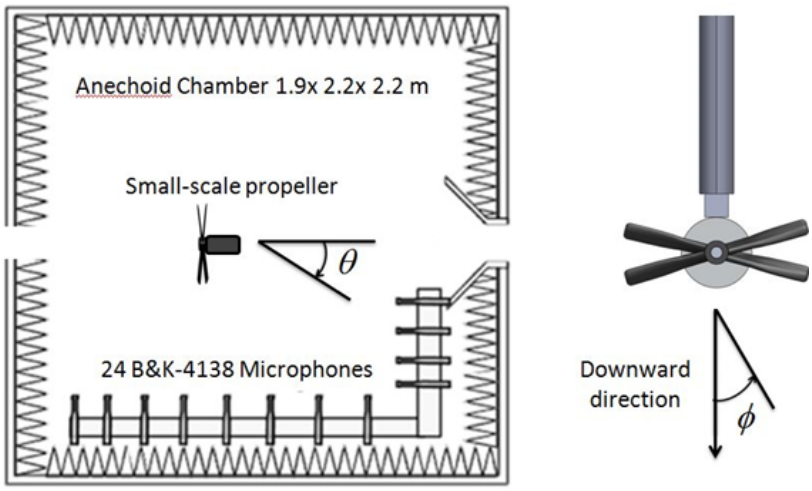

Figure 2.7: The experimental setup from [9]

angle on the individual propeller thrust was studied. Particularly, it was discovered that the increase in the index angle causes the decrease of lower propeller thrust, while the upper propeller thrust is increased.

Kim investigated the acoustic characteristics of a four-bladed rotor with uneven blade spacing [9]. The study was conducted in an anechoic chamber, where acoustic pressure was measured using 24 microphones (Fig 2.7). The results showed that rotors with uneven blade spacing generated less thrust than rotors with evenly space blades at the same RPM. Kim suggested that in coaxial rotor configurations, the twist distribution must be adjusted, to mitigate thrust loss. When the distance between the rotors is small, the downwash from the leading blade interacts with the trailing blade and reduces its effective angle of attack. The trailing blade generates significantly less lift than expected. The study found that the increase in broadband noise levels in unevenly spaced blades was associated with small axial spacing. In Kim's experiment, the blades were mounted on a single hub and merged near the root, which increased the broadband noise. However, when the blades were placed on two separate hubs with increased axial spacing, the broadband noise did not increase. Additionally, rotors with uneven blade spacing produced twice as many tonal peaks as coplanar rotors. However, these tones were shifted to lower frequencies, leading to a reduction in A-weighted noise levels.

Grande et al. investigated the stacked 2×2 bladed propeller in hover conditions comparing it to 4- and 2-bladed propellers [25]. The upper rotor generated significantly more thrust than the lower rotor, aligning with the findings in [24]. However, in contrast to [24], Grande et.al found that the increase of the index angle causes the upper rotor thrust to decrease, while the lower rotor thrust is increased. The total thrust of stacked rotors was higher than the thrust of the 4-bladed coplanar rotor.

2.6 Summary

Table 2.1 presents the summary of the research studies on stacked rotors. Previous research showed that the axial distance and the separation angle between the rotors are the two crucial parameters that influence the aerodynamic and aeroacoustic performance of the stacked rotors. However, it has been shown in numerous studies that the index angle has the greatest impact on acoustic performance, mostly due to its influence on loading noise caused by the aerodynamic interactions in the flow. Moreover, the effect of the index angle tends to diminish as the axial distance increases.

While previous studies provided valuable insights into the acoustic performance of stacked rotors, limited research has focused on the tonal noise modulation by the index angle variation. This thesis addresses this gap through unsteady CFD simulations and acoustic analysis. This study will provide a deeper understanding of how changes in rotor configuration influence the modulation of sound. Further research is required to determine the optimal configuration of the stacked rotor, that minimizes noise while preserving aerodynamic efficiency.

Table 2.1: Summary of research studies on stacked rotors.

#	Authors, year	Methods	Design variables	Main findings
1	Daiju Uehara and Jayant Sirohi (2017)	Experimental study	Index angle	• Configurations with positive index angle (upper blade leading) had the best aerodynamic performance.
2	Charles E. Tinney and John Valdez (2019)	Experimental study	Index angle, axial distance	• Index angle had a bigger effect on acoustic performance than axial distance.
3	Siena K. S. Whiteside et al. (2019)	CFD and experimental study	Index angle, axial distance	• The configuration with the leading lower rotor was the most aerodynamically efficient. • Stacked rotors produce less broadband noise compared to a coplanar rotor.

#	Authors, year	Methods	Design variables	Main findings
4	George Jacobellis et al. (2021)	CFD and experimental study	Index angle, axial distance	• A significant difference in thrust between lower and upper rotor in configurations with small index angle • 10 % thrust reduction at zero index angle
5	Yoonpyo Hong et al. (2023)	CFD and neural network optimization	Index angle, axial distance, and pitch angle difference	• Index and pitch angles have little effect on the aerodynamic performance in configurations with big axial distance. • BVI increased local power loading of the lower rotor.
6	Stefan Platzer et al. (2023)	CFD and experimental study	Index angle	• Increasing the index angle decreases the thrust of the lower rotor while increasing the thrust of the upper rotor. • The trajectories of the tip vortices are significantly affected by the index angle.
7	Edoardo Grande et al. (2024)	CFD (Lattice-Boltzmann simulations)	Index angle, axial distance	• The induced flow created by the lower rotor accelerates the vortices from the upper rotor in the downward direction, which leads to the BVI on the lower rotor. • Stacked configurations produced more tonal noise than the single coplanar rotor.

Chapter 3

Methodology

3.1 Overview

This chapter will be dedicated to the methodology employed in this study, outlining main approaches and assumptions. The APC 27×13 rotor, shown in Figure 3.1, was used in this study. It has a diameter of 0.6858 m and pitch of 0.3302 m. The chord and twist distributions of the rotor are presented in Figure 3.2.

Figure 3.1: APC 27×13 propeller, [10].

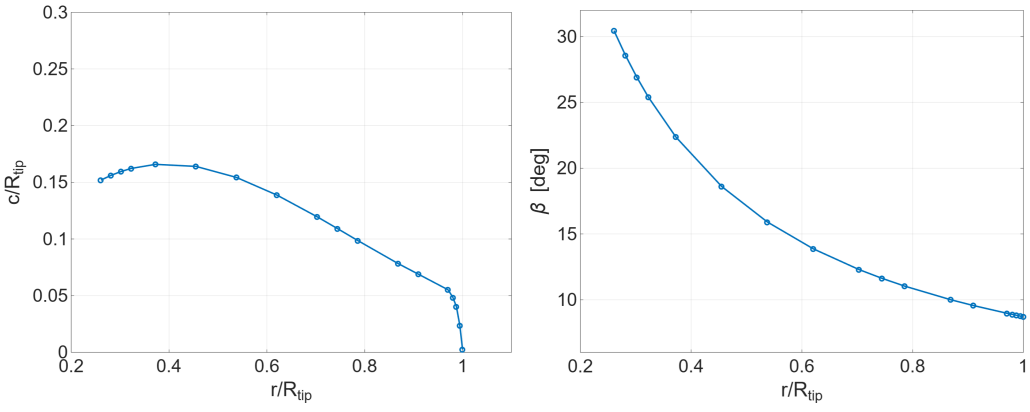

(a) (b)

Figure 3.2: Rotor geometry: a) rotor chord distribution; b) rotor twist distribution

In order to investigate the influence of the index angle and axial distance on the noise levels, six stacked rotor configurations were constructed with three varying stacking distances and two index angles (Table 3.1).

Table 3.1: Configurations of the tested rotors.

#	Axial Spacing	Index Angle
1	0D	90°
2	0D	30°
3	0.25D	90°
4	0.25D	30°
5	0.5D	90°
6	0.5D	30°

where D is the rotor diameter.

The testing of each configuration involved the use of both CFD simulation and acoustic examination. The methodology scheme is presented on Figure 3.3. The CFD simulations were carried out using the OpenFoam software and the acoustic examination was performed using PSU-WOPWOP.

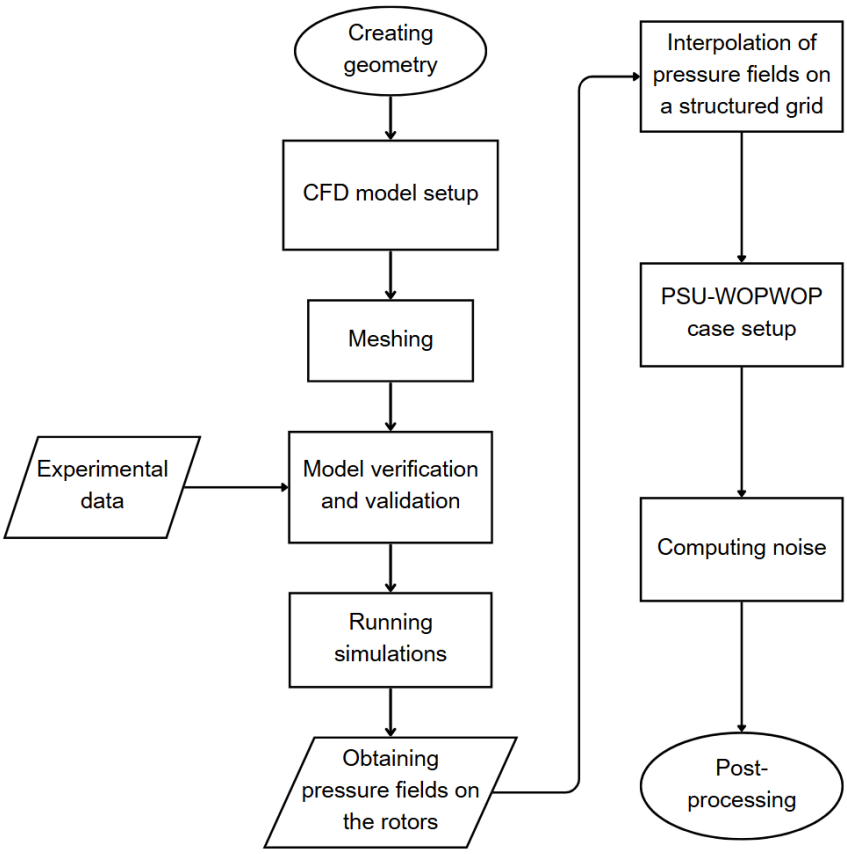

Figure 3.3: Methodology overview.

3.2 CFD Simulations

3.2.1 OpenFoam Setup

The open-source computational fluid dynamics (CFD) software OpenFOAM (Open Field Operation and Manipulation) [11] was used for the aerodynamic simulations in this study. It provides a flexible environment for simulating complex fluid dynamics problems and offers a wide variety of solvers and utilities. Unlike commercial software, OpenFOAM provides its users with the opportunity to modify and refine solution algorithms to suit specific requirements. The typical structure of the OpenFOAM case with directory descriptions is presented in the figure below.

```
<case>
├── 0.orig (contains files with boundary conditions for each variable)
│   └── ...
├── constant
│   ├── geometry
│   ├── polyMesh (mesh files)
│   ├── dynamicMeshDict (dynamic mesh settings)
│   ├── transportProperties (physical properties)
│   └── momentumTransport (turbulence properties)
├── system
│   ├── controlDict (run control parameters)
│   ├── blockMeshDict (meshing parameters)
│   ├── snappyHexMesh (meshing parameters)
│   ├── createBafflesDict (baffles creation)
│   ├── decomposeParDict (parallel run parameters)
│   ├── surfaceFeaturesDict (generate surface features)
│   ├── forces (post-processing)
│   └── ...
└── <time directories>
```

Figure 3.4: Case structure in OpenFOAM

The rotation of the rotors was implemented using two different approaches: Multiple Reference Frame (MRF) approach and sliding mesh approach. The Multiple Reference Frame approach is a steady-state method used in CFD to model the rotation without physically moving the mesh. In MRF simulation the computational domain is split into two reference frames: stationary zone and the rotating zone that contains the rotor. The governing equations are modified by introducing additional source terms that account for the effects of rotation. MRF approach is computationally effective and easy to implement. However, this method does not allow to capture transient phenomena like vortex-blade interaction, which is crucial for rotor simulations.

Unlike MRF, sliding mesh approach physically rotates the mesh at the given angular speed. In OpenFoam sliding mesh is implemented using Arbitrary Mesh Interface (AMI) technique. AMI allows to perform simulation across disconnected, but adjacent meshes

[11]. In the case of rotor, the stationary mesh zone contains a rotating cylindrical region within itself. AMI creates an interface between two meshes that exchange variables between rotating and non-rotating regions. Since sliding mesh simulates the physical rotation, it is able to capture transient phenomena. However, it is more computationally expensive than MRF due to time-dependent mesh updates.

3.2.2 Governing Equations

The cross section of the computational domain is presented on Figure 3.5.

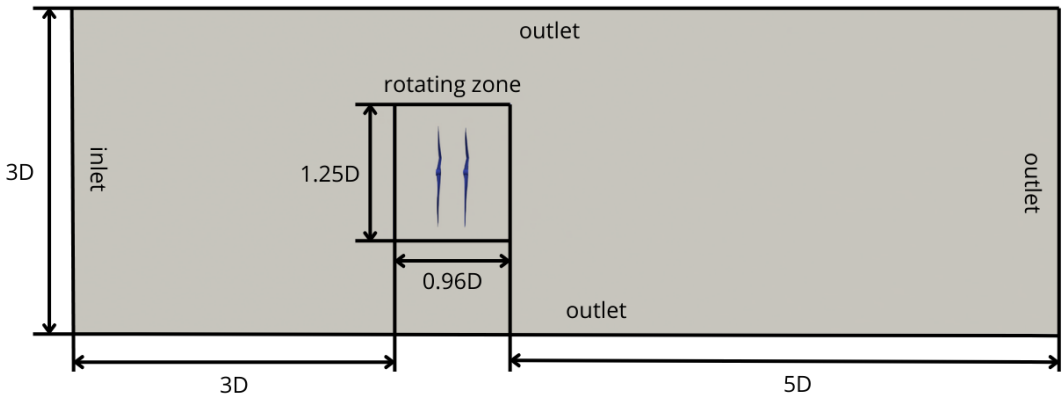

Figure 3.5: Computational domain.

The governing equations for the simulation are unsteady, incompressible Reynolds averaged Navier-Stokes equations. The $k-\omega$ turbulence model was used [26]. The continuity and momentum equations are given by equations 3.1 and 3.2.

$$\frac{\partial \overline{u_i}}{\partial x_i} = 0 \tag{3.1}$$

$$\frac{\partial \bar{u}_i}{\partial t} + \bar{u_j}\frac{\partial \bar{u}_i}{\partial x_j} = -\frac{1}{\rho}\frac{\partial \bar{p}}{\partial x_i} + \nu\frac{\partial^2 \bar{u}_i}{\partial x_j \partial x_j} - \frac{\partial \overline{u_i' u_j'}}{\partial x_j} \tag{3.2}$$

where $\overline{u_i}$ is the mean velocity component, $\overline{p}$ is the mean pressure, ρ - is the id density, $\nu = \mu/\rho$ - kinematic viscosity, $\overline{u_i' u_j'}$ - Reynolds stresses.

The transport equations for turbulence kinetic energy and turbulent dissipation rate are given by equations 3.3 and 3.4:

$$\frac{\partial(\rho k)}{\partial t} + \nabla \cdot (\rho \bar{u} k) = \nabla \cdot \left(\left(\mu + \frac{\mu_t}{\sigma_k}\right)\nabla \cdot k\right) + p_k - \rho\varepsilon \tag{3.3}$$

$$\frac{\partial(\rho \omega)}{\partial t} + \nabla \cdot (\rho \bar{u} \omega) = \nabla \cdot \left(\left(\mu + \frac{\mu_t}{\sigma_\omega}\right)\nabla \cdot \omega\right) + \frac{\gamma}{\nu_t} p_k - \beta\rho\omega^2 \tag{3.4}$$

where k is the turbulence kinetic energy, ω is the specific turbulence dissipation rate, $\varepsilon = \omega k C_\mu$ is the turbulence dissipation rate, μ is the dynamic viscosity, μ_t - turbulent

viscosity. The empirical coefficients are: $\sigma_k = 0.5$, $\sigma_\omega = 0.5$, $\beta = 0.072$, $\gamma = 0.52$, $C_\mu = 0.09$ [27].

The velocity-inlet is specified at the left wall to represent the incoming flow:

$$U = 10\,m/s, \quad \frac{\partial p}{\partial x} = 0 \tag{3.5}$$

The boundary setting at the right wall and the cylinder walls switches between two boundary conditions depending on the flux sign. When the inflow is present the velocity is obtained from patch-face normal component of the internal-cell value. For the outflow a zero-gradient boundary condition is applied:

$$\frac{\partial U}{\partial x} = 0 \tag{3.6}$$

This was achieved using OpenFoam's *pressureInletOutletVelocity* boundary condition.

The initial turbulence kinetic energy and specific turbulence dissipation rate fields were calculated using equations 3.7. These values were uniform across the computational domain.

$$k = \frac{3}{2}(UI)^2, \omega = \frac{C_\mu^{-\frac{1}{4}} k^{\frac{1}{2}}}{l} \tag{3.7}$$

where the turbulence intensity was set to $I = 3\,\%$, and the turbulence length scale was defined as $l = 0.07D$.

3.2.3 Mesh Generation

The mesh was generated using OpenFoam's internal meshing tools. The static domain of the mesh was constructed using "blockMesh". Geometry files for inner domain (AMI.stl) and rotor (fan.stl) were created separately and stored in *\constant\geometry*.

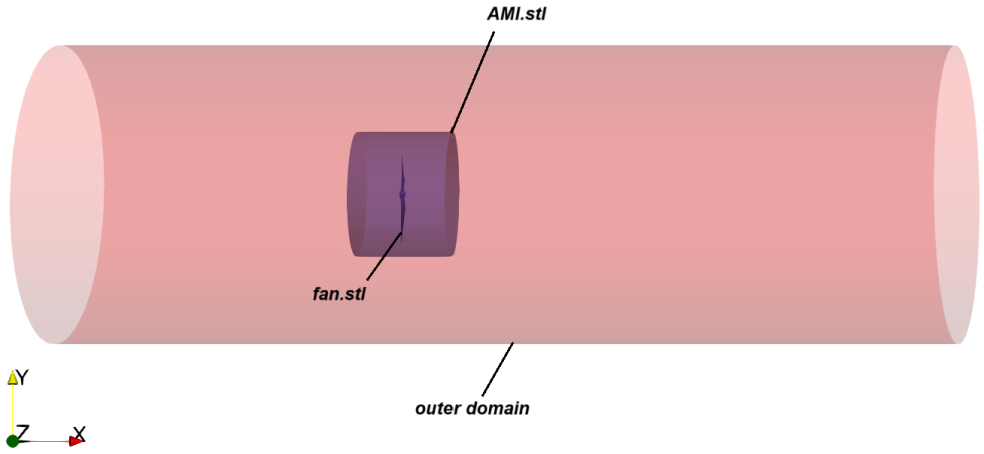

Figure 3.6: Geometry layout.

The mesh refinement was applied to surface features and STL surfaces using snappyHexMesh. To improve numerical efficiency, the mesh was renumbered to

increase bandwidth. The interfaces between the outer domain and AMI were created using "createBaffles" utility. The parameters of the interfaces were specified in the "createBafflesDict". The interfaces were split to allow the sliding of the mesh using "splitBaffles". The mesh for one of the configurations is presented on Figure 3.7. The computed y^+ values were within the acceptable range for the $k-\omega$ turbulence model, indicating sufficient near-wall resolution.

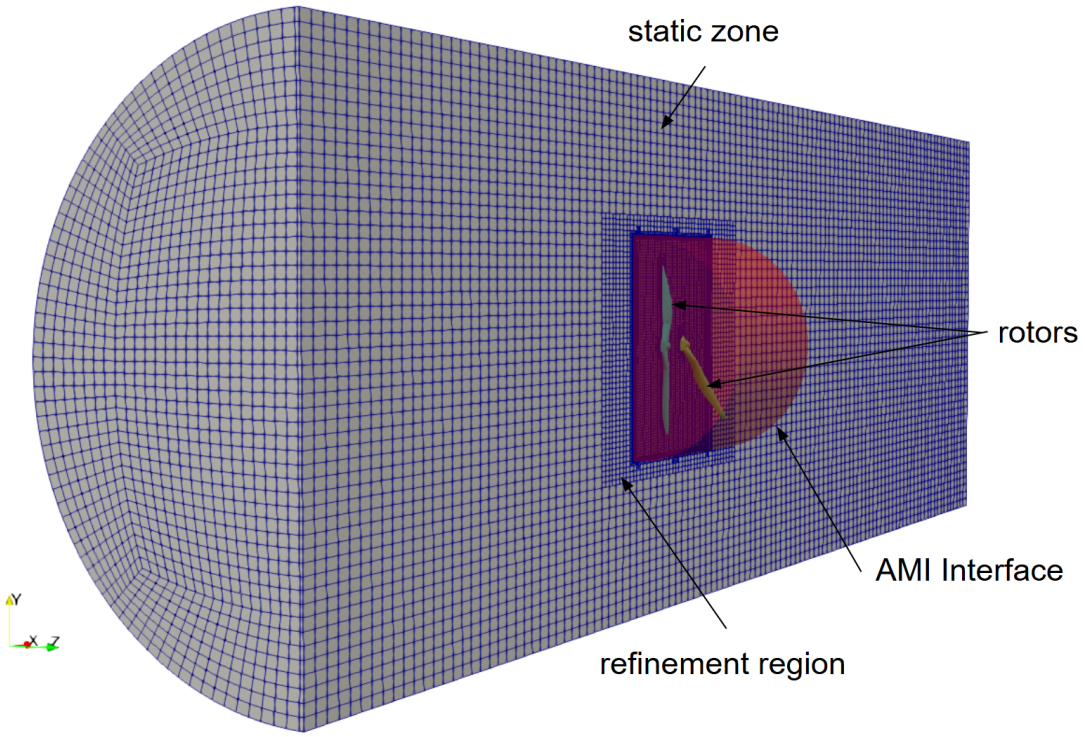

Figure 3.7: Mesh for a $\Delta\phi = 30°$, $\Delta x = 0.25D$ configuration

3.2.4 Solver

The **pimpleFOAM** solver was used to carry out the CFD simulations. This solver is based on the PIMPLE algorithm, which is a combination of PISO (Pressure Implicit with Splitting of Operators) and SIMPLE (Semi-Implicit Method for Pressure-Linked Equations) [28] algorithms for pressure-velocity coupling. The time step was calculated using $\delta t = \frac{Co \cdot \delta x}{|\mathbf{U}|}$. The Courant's number was set to 0.8. Figure 3.8 illustrates the flowchart of the PIMPLE algorithm including the energy equation, which was not used in this study.

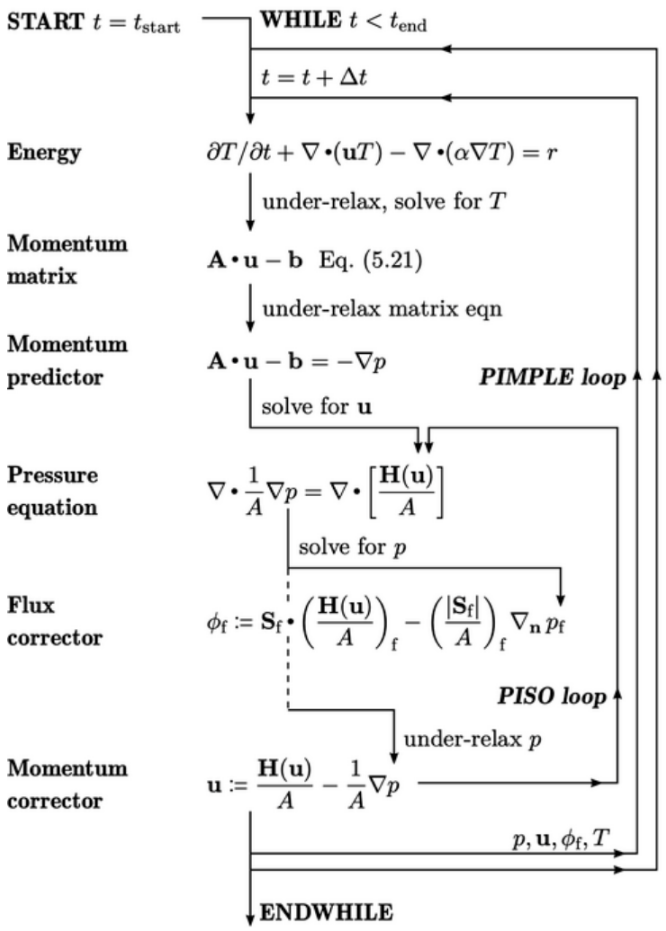

Figure 3.8: PIMPLE algorithm, [11].

3.2.5 Post-Processing

Because the sliding mesh simulation is inherently transient, it captures the time-dependent pressure field on the surface of the blades. As a result, the computed thrust is unsteady and varies with the rotor's angular position. A time-averaged thrust value was obtained to represent mean thrust coefficient.

Figure 3.9 illustrates the unsteady thrust generated during the simulation of a two-bladed rotor at 3000 RPM. During the first two periods of rotation (0–0.04 s), a transient phase can be observed. After this initial period, the thrust coefficient (C_T) fluctuates within a small range.

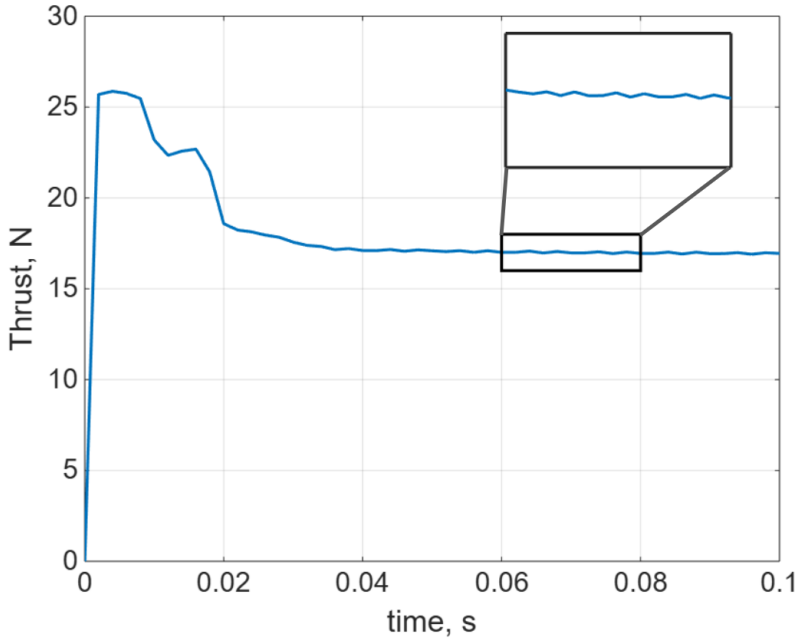

Figure 3.9: The change in thrust generated by the rotor over time at $J = 0.3$

The thrust is computed by integrating the mean pressure projected onto the unit normal vector across the rotor surface. It was averaged over one full revolution after the rotors achieved five revolutions. Thrust coefficient was calculated using equation (3.8):

$$C_T = \frac{T}{n^2 D^4 \rho} \tag{3.8}$$

where T is the thrust and n - rotations per second. The advance ratio was determined using equation 3.9:

$$J = \frac{V_{inlet}}{nD} \tag{3.9}$$

3.2.6 Grid Sensitivity Study

To validate numerical model, grid sensitivity study was performed using a 2-bladed configuration. The results for simulations with $J = 0.3$ are presented in Table 3.2. The C_T difference between the two finer meshes was less than 5 %. Figure 3.10 illustrates the variation in C_T differences across a range of advance ratios.

Table 3.2: OpenFoam grid sensitivity ***($J = 0.3$).***

Number of Elements	C_T	Relative Error (%)
790,416	0.037	
903,920	0.0429	13.7%
1,103,243	0.044	2.43%

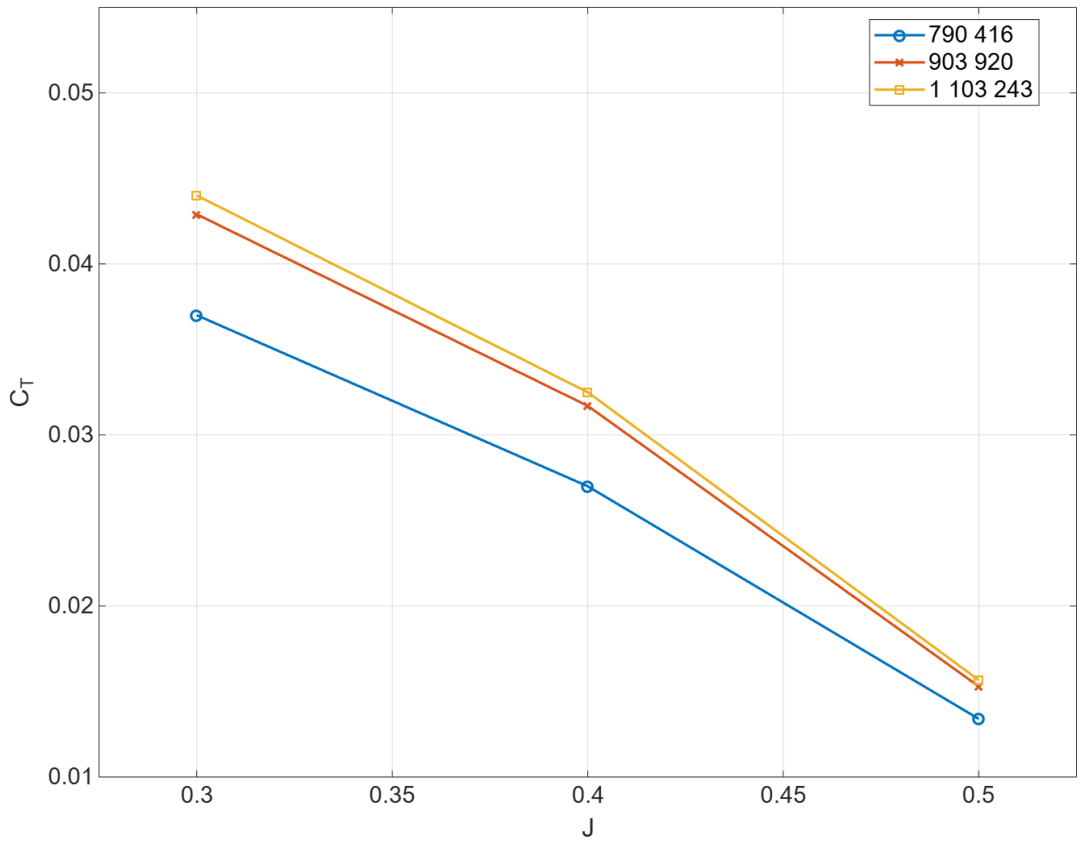

Figure 3.10: OpenFoam grid independence study.

3.2.7 Model Validation

The experimental data provided by the manufacturer [12] were used to validate the numerical results for a 2-bladed rotor.

Figure 3.11 shows a comparison of thrust coefficient curves obtained from the experiment and this thesis. Additionally, results for a MRF simulation from [13] is presented. Both the simulations and the experiment were conducted at 5000 RPM. Deviations of up to 25% can be observed. The significant difference in the advance ratio (J) is expected, as the blades are operated in static conditions. To match the advance ratio, different inflow velocities were numerically prescribed. Difference between the simulated and experimental inflow conditions can have a significant effect on the results. These discrepancies highlight the sensitivity of thrust predictions to inflow characteristics and boundary conditions. Improving the experimental setup could help reduce the gap between simulated and measured performance. Nevertheless, the thrust coefficient trend shows good agreement with the experimental results. For future work, a rotor with better experimental data must be considered.

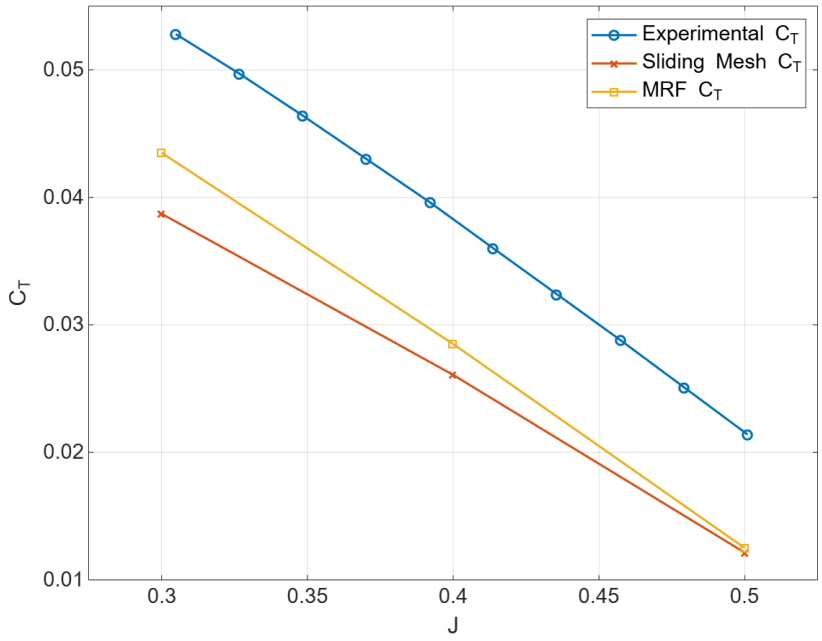

Figure 3.11: Comparison of thrust coefficient with experimental data [12] and MRF simulation [13].

Additionally, the configuration with $\Delta\phi = 30°$, $\Delta x = 0D$ was analyzed across various advance ratios to assess its aerodynamic performance. To achieve the desired advance ratios, the inlet velocity was fixed at $U_{inlet} = 10\ m/s$ while the rotational speed of the rotors was varied. A comparison with the results from [13] shows, that the difference in thrust coefficients is more significant at lower advance ratios, as shown in Figure 3.12.

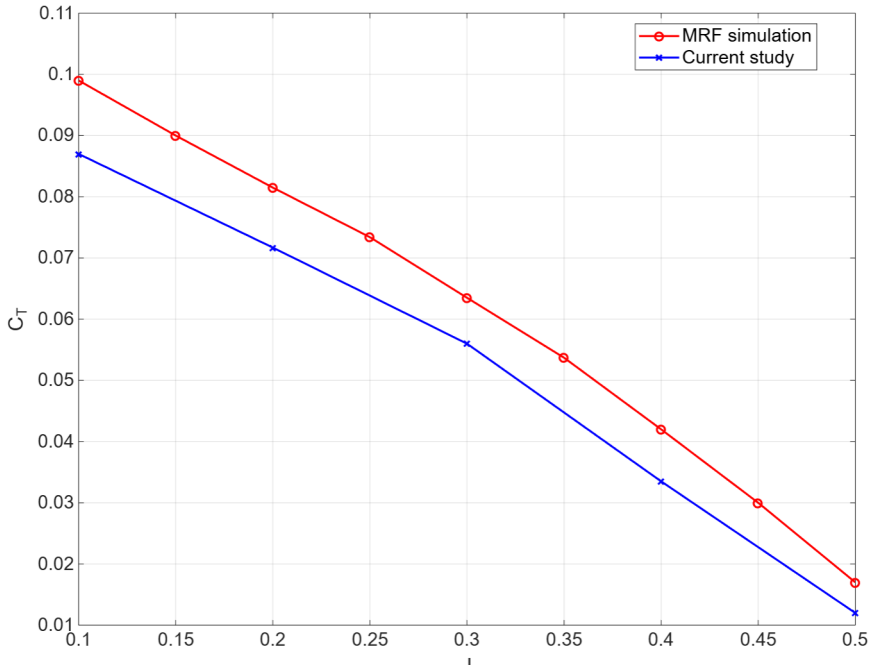

Figure 3.12: Thrust coefficient comparison for a $\Delta\phi = 30°$, $\Delta x = 0D$ configuration

3.3 Aeroacoustic Simulations

3.3.1 Farassat's Formulation 1A

The solution to FW-H equation was proposed by Farassat as a time-domain integral formulation [29]. It describes the sound produced by a moving surface as the sum of monopole and dipole terms. As previously mentioned, computing a quadrupole term is computationally expensive; therefore it is not included in the formulation. Equations (3.10)- (3.12) are known as Farassat's Formulation 1A. The acoustic pressure is decomposed into:

$$p'(\vec{x},t) = p'_T(\vec{x},t) + p'_L(\vec{x},t) \tag{3.10}$$

where p'_T represents the monopole term, that generates thickness noise, and p'_L is the dipole term, responsible for loading noise. The terms are computed from:

$$\begin{aligned} p'_T(\vec{x},t) = &\frac{1}{4\pi}\int_{f=0}\left[\frac{\rho_0(\dot{v_n}+\dot{v_{\dot{n}}})}{r\left|1-M_r\right|^2}\right]_{ret} dS \\ &+\frac{1}{4\pi}\int_{f=0}\left[\frac{\rho_0 v_n(r\dot{M}_r + c_0 M_r - c_0 M^2)}{r^2\left|1-M_r\right|^3}\right]_{ret} dS \end{aligned} \tag{3.11}$$

$$\begin{aligned} p'_L(\vec{x},t) = &\frac{1}{4\pi c}\int_{f=0}\left[\frac{\dot{l_r}}{r\left|1-M_r\right|^2}\right]_{ret} dS \\ &+\frac{1}{4\pi}\int_{f=0}\left[\frac{l_r - l_M}{r^2\left|1-M_r\right|^2}\right]_{ret} dS \\ &+\frac{1}{4\pi c}\int_{f=0}\left[\frac{l_r(r\dot{M}_r + c_0 M_r - c_0 M^2)}{r^2\left|1-M_r\right|^3}\right]_{ret} dS \end{aligned} \tag{3.12}$$

where $v_i = \frac{\rho}{\rho_0}(v_i - u_i) + u_i$, $l_i = p'\delta_{ij}\hat{n}_j + \rho v_i(v_i - u_i)$, $r = |\vec{x} - \vec{y}|$ is the distance between the observer and the sound source. Due to the propagation delay, the notion of retarded time is introduced in the formulation. The time at the source location (τ) is different from the observer's time and is related to it by the equation (3.13).

$$t = \tau + \frac{r}{c_0} \tag{3.13}$$

3.3.2 PSU-WOPWOP

Acoustic predictions were performed using PSU-WOPWOP, an aeroacoustic solver designed for predicting noise generated by moving rotorcraft. The noise prediction algorithm of PSU-WOPWOP is based on the numerical integration of the Farassat's Formulation 1A of the Ffowcs Williams-Hawkings Equation. The pressure field on the

blades, that was obtained during aerodynamic simulations is used as an input data for PSU-WOPWOP.

The information about the geometry of the rotorcraft is stored in the object called a "patch". A patch represents a single structured surface mesh over which the integration is performed. In this study, each rotor blade was was constructed of two patches: the upper surface and the lower surface. In coplanar rotors, each rotor consisted of four blades, whereas for stacked rotors, there were two 2-bladed rotors. Multiple rotors are combined into objects called "containers", which are recursive objects used to construct various rotor configurations.

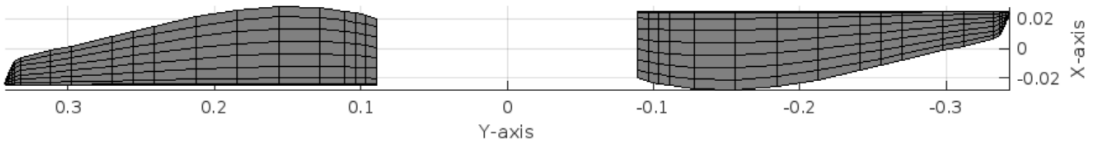

Figure 3.13: Surface mesh for a 2-bladed rotor.

The movement of the blades is implemented using a "change of base". A change of base allows the user to define the transformations of the object, such as rotation of the propeller or forward flight.

An "observer" object determines the locations at which the acoustic pressure is computed. A single case can include multiple observers. Moreover, a change of base can be applied to observers, allowing them to move relative to the rotorcraft if needed. In this study, one observer was positioned within the rotational plane, $5D$ away from the rotor (Figure 3.14).

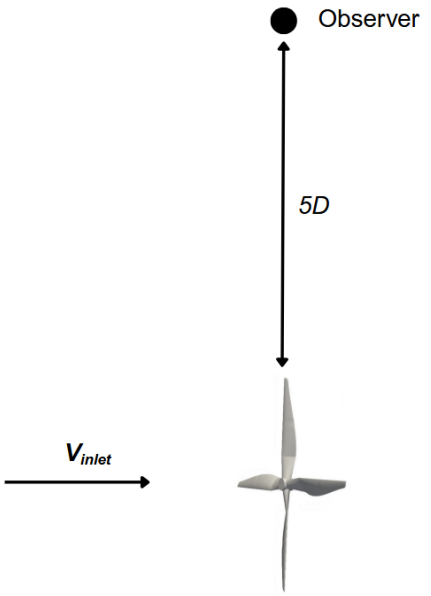

Figure 3.14: Observer.

A typical case structure of the PSU-WOPWOP is illustrated on the figure below.

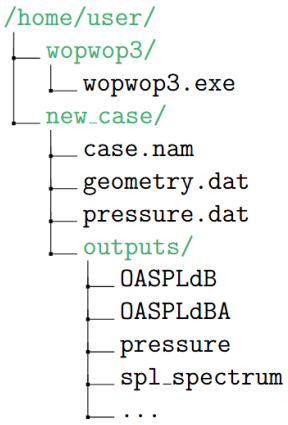

Figure 3.15: Case structure of the PSU-WOPWOP

The structured mesh and the pressure information of the patch are stored in the binary files *geometry.dat* and *pressure.dat*. A namelist file *case.nam* contains the information about the environment, patches, observers, and containers. The user specifies the desired output within this file, such as the frequency spectrum, OASPL in dB and dBA, acoustic pressure, audio files, etc.

3.3.3 Grid Sensitivity Study

The PSU-WOPWOP grid independence study was conducted using results obtained from an MRF simulation. Figure 3.16 presents the pressure distribution interpolated on three grids with varying densities.

Table 3.3: PSU-WOPWOP grid sensitivity.

Number of Elements	Relative Error (%)
144	
324	9.6%
576	1.23%

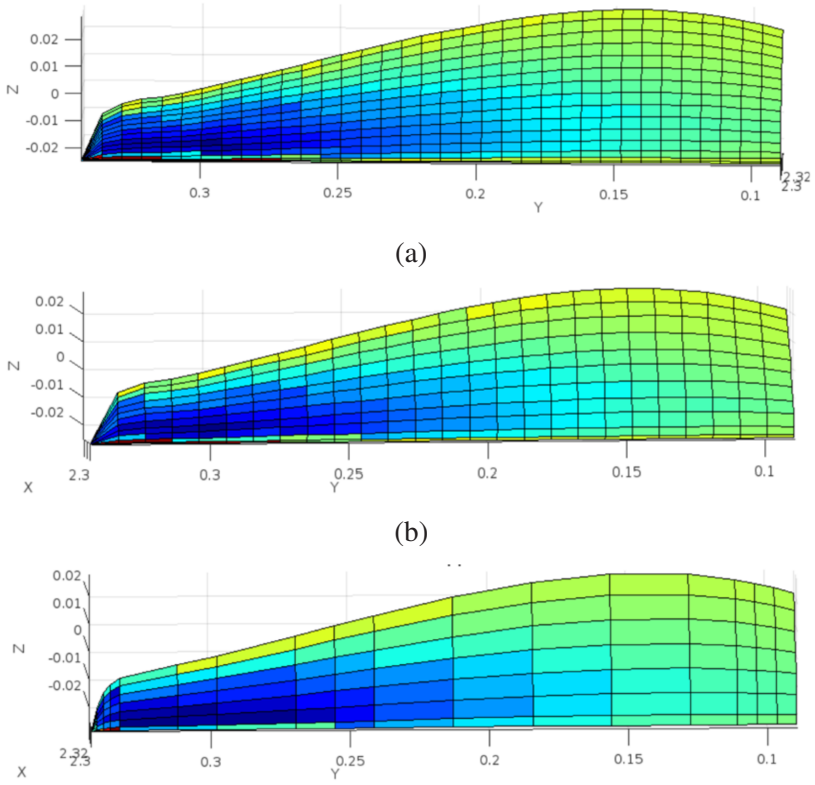

Figure 3.16: Grid sensitivity study: a) 576 elements; b) 324; c) 144

Figure 3.17 presents the total acoustic pressure for the coplanar 4-bladed rotor across the tested grids. Based on the results of this study, the 324-element grid was selected for further simulations.

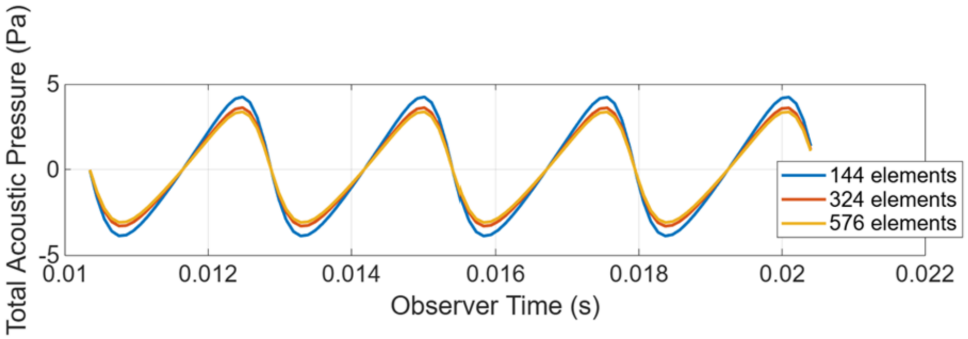

Figure 3.17: Grid sensitivity study.

Chapter 4

Results

4.1 Aerodynamic Assessment

All simulations were performed for an advance ratio of $J = 0.1$ as it corresponds to the operating condition with the highest thrust coefficient. To achieve this advance ratio, the inlet velocity was set to $U_{inlet} = 10\ m/s$ and rotational velocity of the rotors was $\omega = 916\ rad/s$ or $8749\ RPM$

Table 4.1 presents the comparison of the thrust coefficient for all configurations relative to the baseline case ($\phi = 90°$, $\Delta x = 0D$). Configurations ($\phi = 90°$, $\Delta x = 0.25D$), ($\phi = 90°$, $\Delta x = 0.5D$) and ($\phi = 30°$, $\Delta x = 0.25D$) showed higher thrust coefficient values than the baseline case. The ($\phi = 30°$, $\Delta x = 0.25D$) configuration was the most efficient among all the tested cases. The lowest C_T was achieved in the coplanar case with $30°$ index angle. This and ($\phi = 30°$, $\Delta x = 0.5D$) configurations exhibited the loss of thrust when compared to the baseline rotor. Overall, the differences were within a small percentage range, demonstrating that the thrust performance does not significantly change between configurations.

Table 4.1: Thrust coefficient difference compared to the baseline rotor $\phi = 90°$**,** $\Delta x = 0D$**.**

Index Angle (ϕ)	Axial Distance (Δx)	C_T	Relative Difference (%)
$90°$	$0.25D$	0.0957	2.9%
$90°$	$0.5D$	0.0948	1.94%
$30°$	$0D$	0.087	6.45%
$30°$	$0.25D$	0.096	3.23%
$30°$	$0.5D$	0.092	1.08%

To further investigate the aerodynamic performance, the Q-criterion isosurfaces colored by velocity were visualized for some of the configurations. Figure 4.1 shows the vortex structures in the flow.

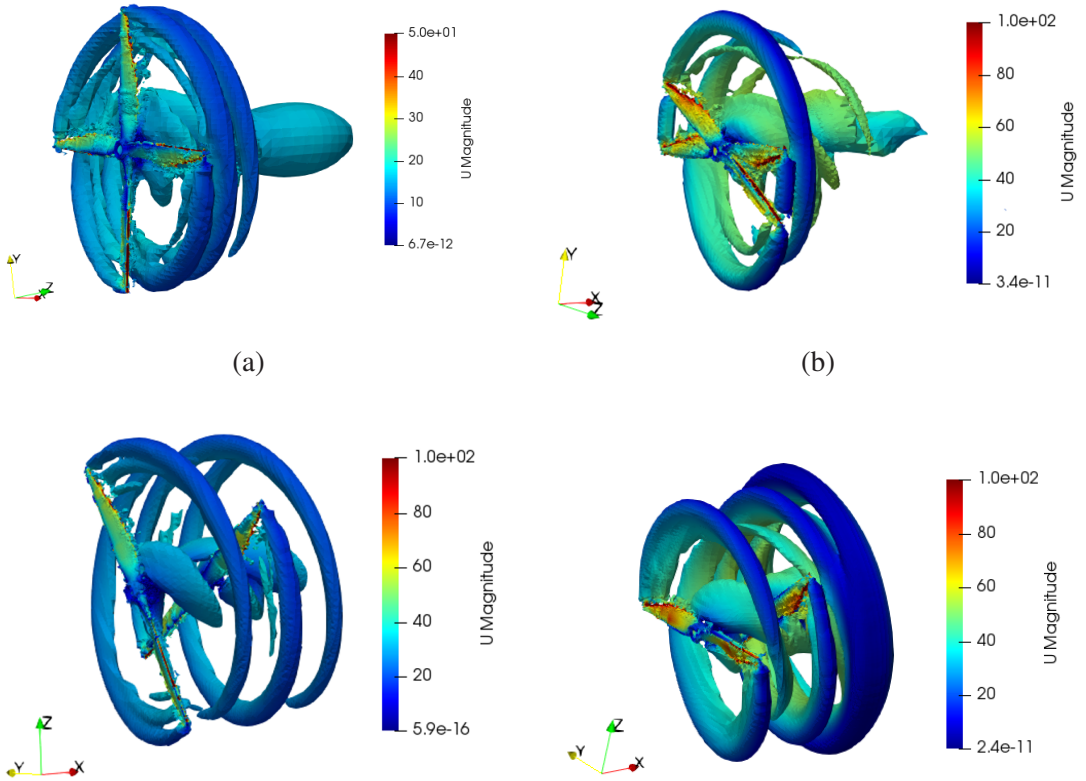

Figure 4.1: Q criterion isosurfaces: a) $\phi = 90°$, $\Delta x = 0D$; b) $\phi = 30°$, $\Delta x = 0D$; c) $\phi = 30°$, $\Delta x = 0.25D$; d) $\phi = 90°$, $\Delta x = 0.25D$

4.2 Acoustic Assessment

4.2.1 Coplanar Configurations

4.2.1.1 Steady-State Comparison

Figure 4.2 presents a comparison of the acoustic pressure obtained using the sliding mesh and MRF approaches [13] for the baseline configuration with $\phi = 90°$ and $\Delta x = 0D$. The plots show the thickness, loading, and total acoustic pressures over one period of rotation. The observer was positioned in the plane of rotation, $5D$ away from the rotor.

A full rotation results in four distinct evenly spaced pressure peaks, each corresponding to a passing blade. The amplitude of the loading acoustic pressure is significantly higher in the sliding mesh simulation, as shown in Figure 4.2b. However, its overall contribution to the total acoustic pressure remains small (Figure 4.2c).

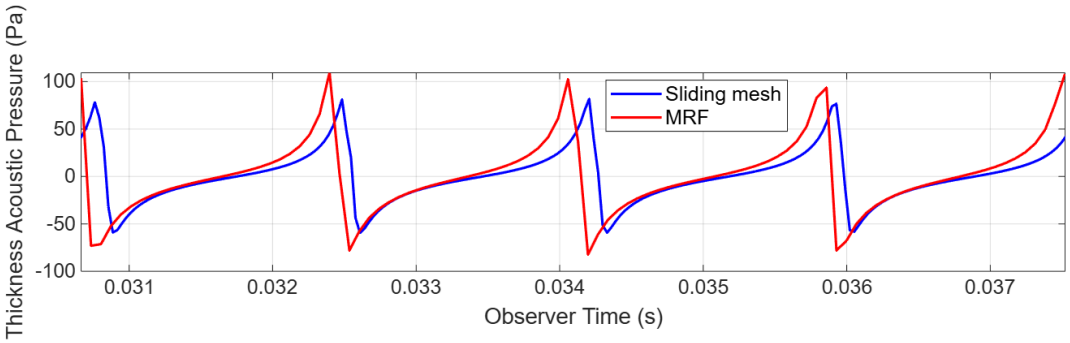

(a) Thickness acoustic pressure

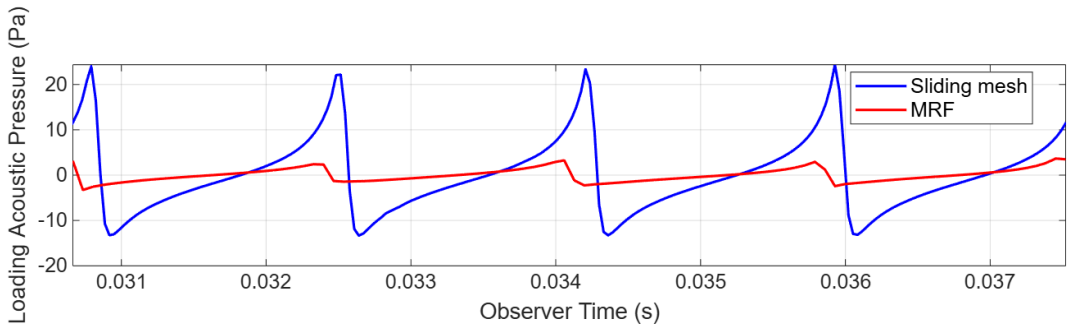

(b) Loading acoustic pressure

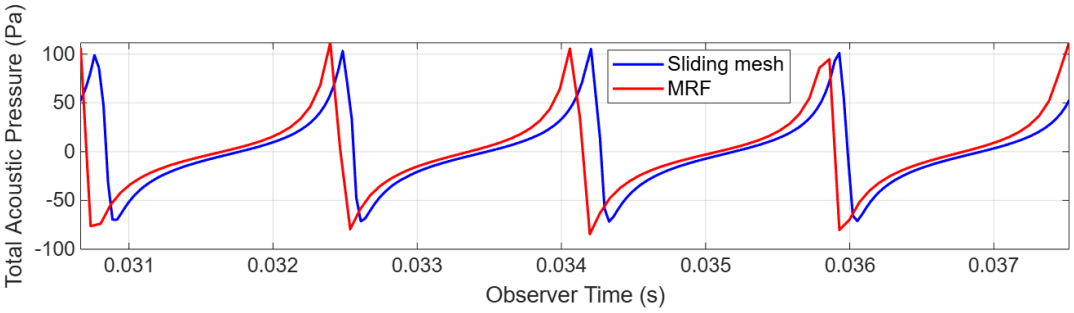

(c) Total acoustic pressure

Figure 4.2: Acoustic pressure comparison between the sliding mesh and MRF approaches for $\phi = 90°$, $\Delta x = 0D$. [13]

Figure 4.3 presents the comparison between the frequency spectra obtained in the current study using the sliding mesh approach and the results reported by [13], using MRF. Noise peaks are observed at every harmonic of the blade passing frequency. This is expected for an evenly spaced rotor due to the periodicity of the blade movement. The peak locations of two simulations coincide at each blade passing frequency (BPF).

The acoustic pressure of the second coplanar configuration with the $30°$ index angle is presented on Figure 4.4. Similar to the configuration with evenly spaced blades, this case shows the increased loading acoustic pressure in the sliding mesh simulation compared to MRF (Figure 4.4b).

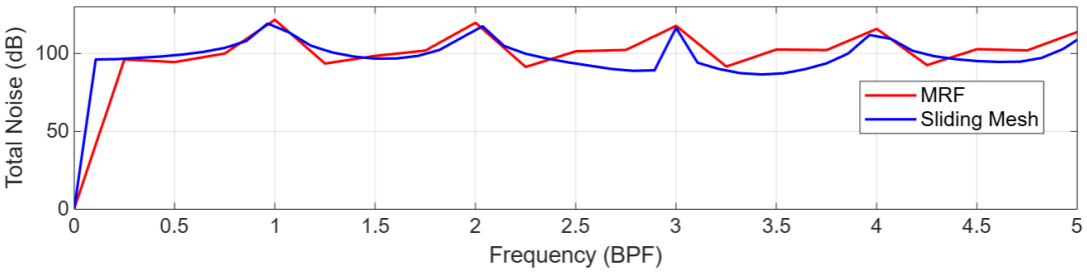

Figure 4.3: Total noise in the $\phi = 90°$, $\Delta x = 0D$ configuration.

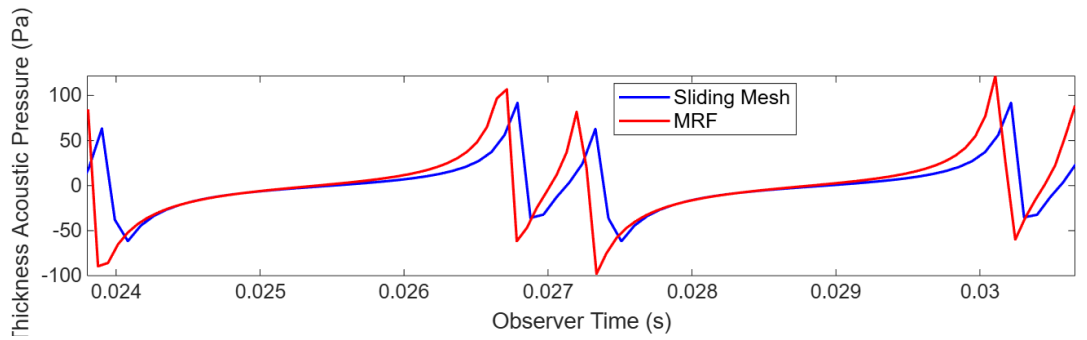

(a) Thickness acoustic pressure

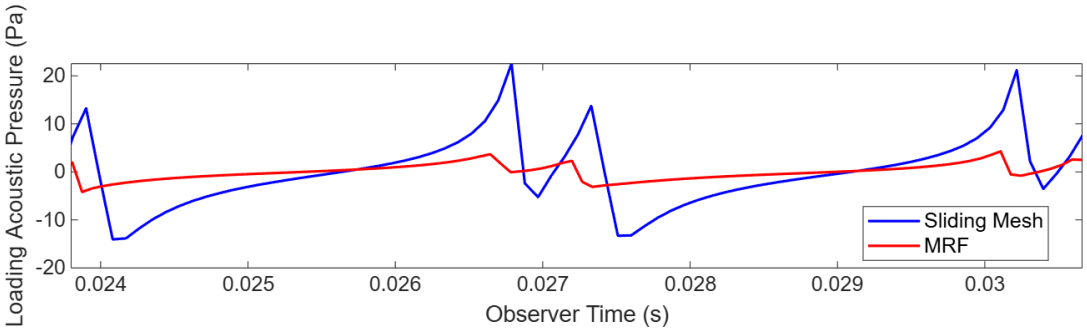

(b) Loading acoustic pressure

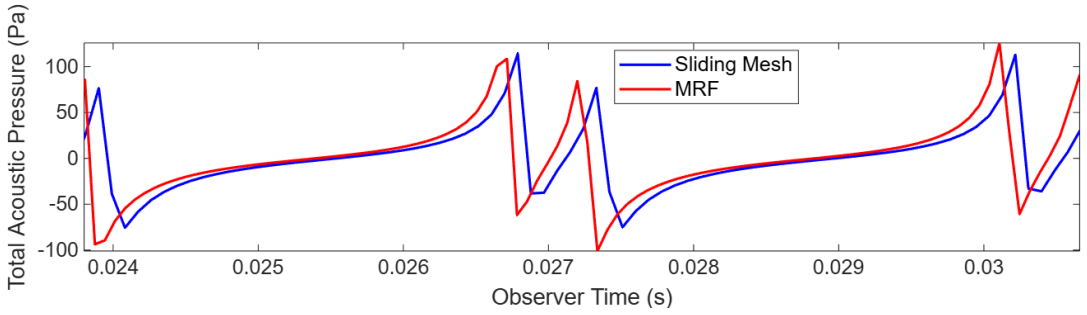

(c) Total acoustic pressure

Figure 4.4: Acoustic pressure comparison between the sliding mesh and MRF approaches for $\phi = 30°$, $\Delta x = 0D$. [13]

The increased loading acoustic pressure in this study is caused by unsteady flow interactions, which cannot be captured in the steady-state MRF simulations. The transient simulations were able to resolve vortex induced noise, resulting in higher loading acoustic pressure levels. However, in both configurations, the loading acoustic

pressure is significantly lower than the thickness pressure and has a minimal contribution to the total acoustic pressure.

4.2.1.2 Effect of Index Angle

The effect of the index angle on the noise was observed in the coplanar cases. The periodicity of pressure peaks changes for the configuration with unevenly spaced blades. Figure 4.5 presents a comparison of the acoustic pressure obtained for the coplanar rotor configurations with $\phi = 90°$ and $\phi = 30°$ over one full rotation. The $\phi = 90°$ case exhibits four evenly spaced peaks, whereas the $\phi = 30°$ configuration produces two dominant peaks followed by two smaller ones. Additionally, the loading acoustic pressure of the first peak is more than three times higher than that of the subsequent peak. However, the total acoustic pressure at the dominant peaks in this configuration aligns with the pressure peaks observed in the evenly spaced rotor.

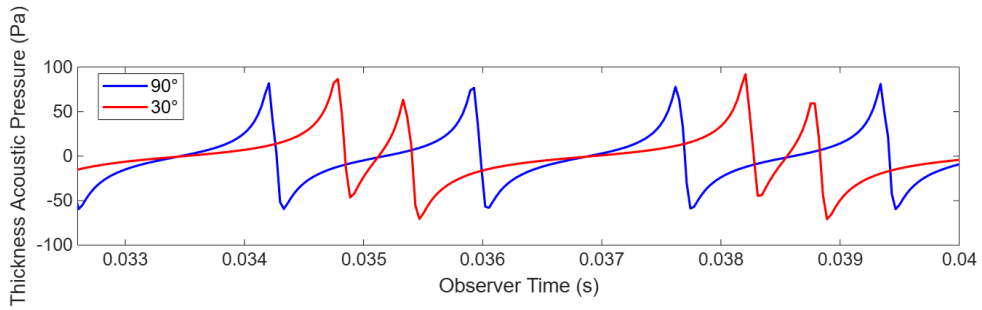

(a) Thickness acoustic pressure

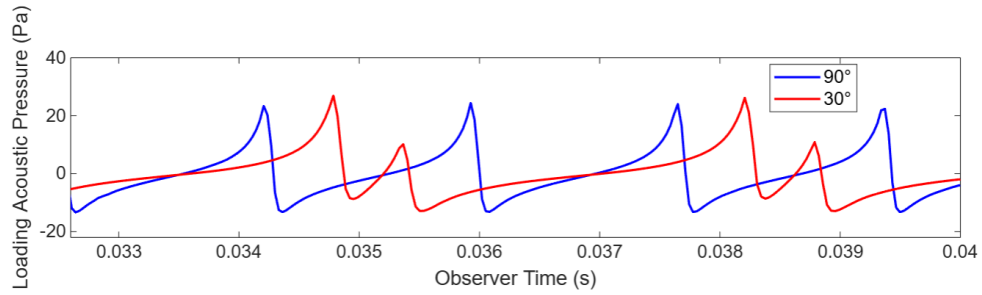

(b) Loading acoustic pressure

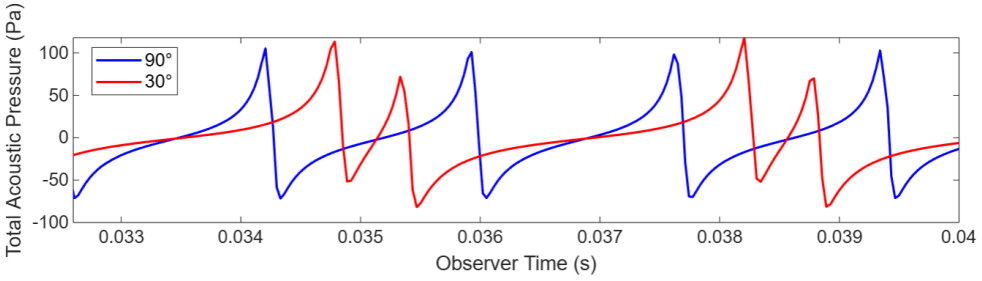

(c) Total acoustic pressure

Figure 4.5: Acoustic pressure comparison at 90° and 30° index angles for 0D axial separation.

The impact of the index angle can be also observed in the frequency spectra for two coplanar configurations (Figure 4.6). The $\phi = 30°$ configuration produces more tonal peaks. While the $\phi = 90°$ case shows peaks at integer multiples of the BPF, the $\phi = 30°$ rotor generates additional peaks at half-integer BPF.

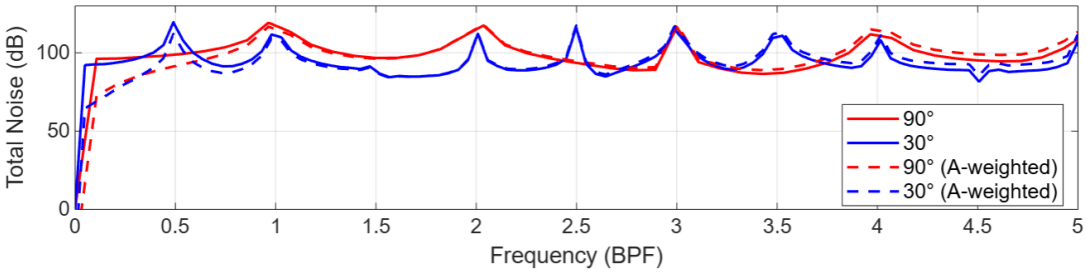

Figure 4.6: Total noise in the coplanar configurations.

4.2.2 Effect of Axial Spacing

Figure 4.7 demonstrates the comparison of total acoustic pressure for the baseline and axially spaced configurations. The results indicate no significant difference in total acoustic pressure between these configurations.

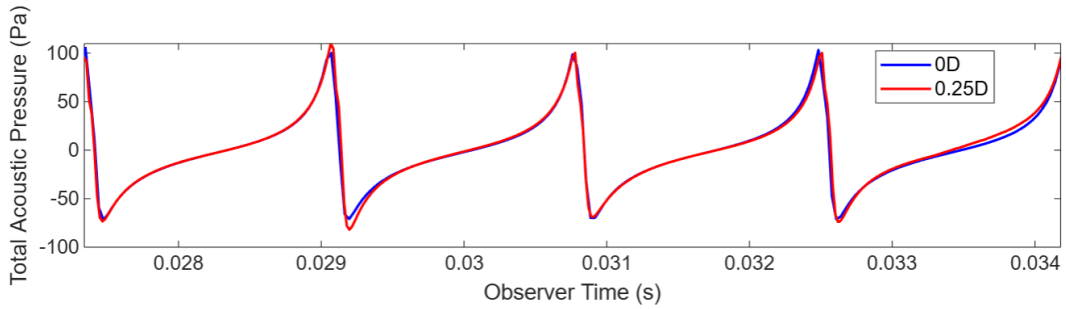

Figure 4.7: Total acoustic pressure for the evenly spaced configuration at $\Delta x = 0$ and $\Delta x = 0.25D$.

However, the axial distance between the rotors influenced the loading acoustic pressure in both the $\phi = 90°$ and $\phi = 30°$ configurations. As shown on Figure 4.8a, increasing the axial distance reduced the loading acoustic pressure for evenly spaced rotors. The same behaviour was also observed in the larger peak of the $\phi = 30°$ configurations (Figure 4.8b). However, coplanar rotor exhibited the lowest loading acoustic pressure at the smaller peak.

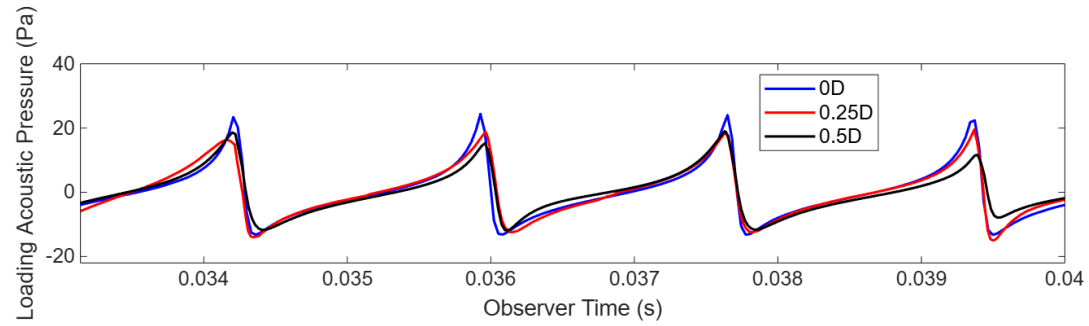

(a) $\phi = 90°$

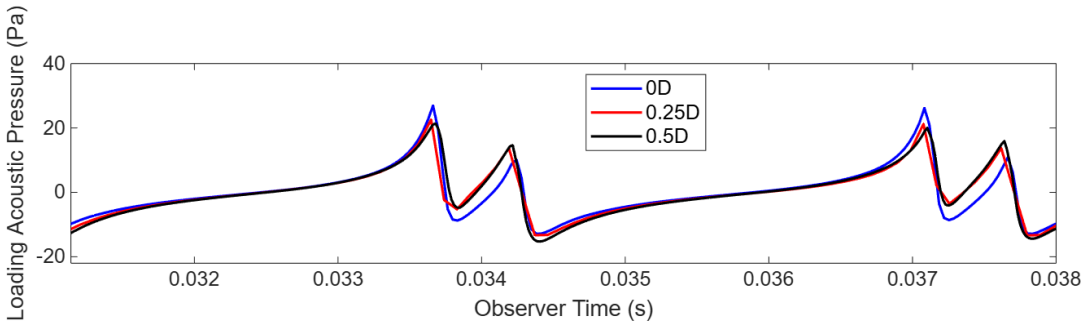

(b) $\phi = 30°$

Figure 4.8: Loading acoustic pressure comparison for $\phi = 90°$ and $\phi = 30°$ configurations.

4.2.3 Combined Effect of Index Angle and Axial Spacing

Figure 4.9a presents the comparison of A-weighted total noise levels for three axial distances in the $\phi = 90°$ configuration. Both $0D$ and $0.25D$ configurations exhibit noise peaks at the two first BPF frequencies. However, the $0.5D$ configuration shows its first peak around $2.4BPF$.

An increase of the axial distance in the configurations with $\phi = 30°$ reduces the number of peaks in the frequency spectrum, as shown in Figure 4.9b. Among these configurations, the rotor with $\Delta x = 0.5D$ demonstrated the lowest A-weighted total noise level at the observer location, as illustrated in Figure 4.9b.

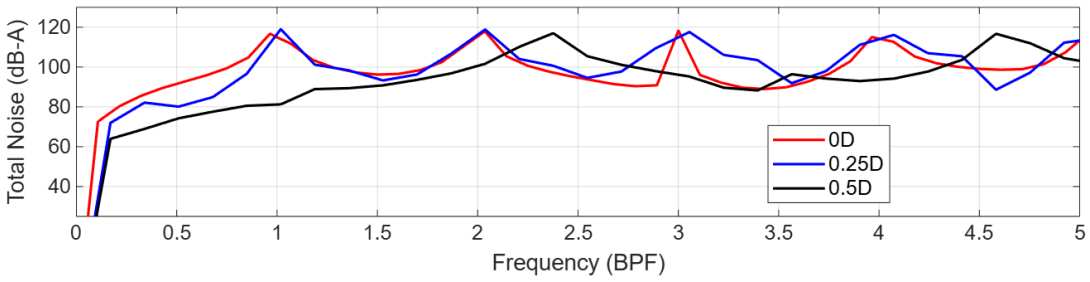

(a) $\phi = 90°$

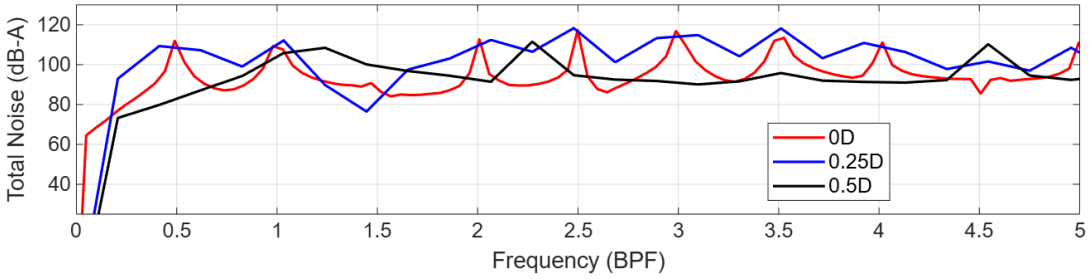

(b) $\phi = 30°$

Figure 4.9: Comparison of frequency spectra for $\phi = 90°$ and $\phi = 30°$ configurations.

As shown in Figure 4.10, the configurations with $\phi = 30°$ produced approximately the same level of loading acoustic pressures across different stacking distances. Furthermore, the impact of the index angle on the loading acoustic pressure does not diminish with an increase in axial distance.

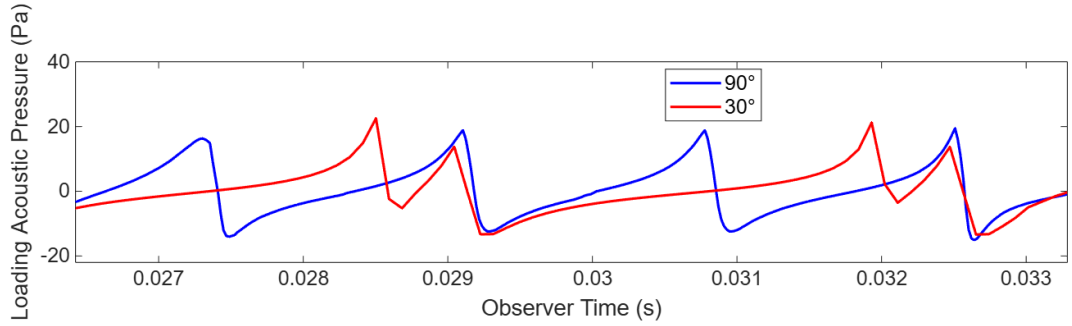

(a) $\Delta x = 0.25D$

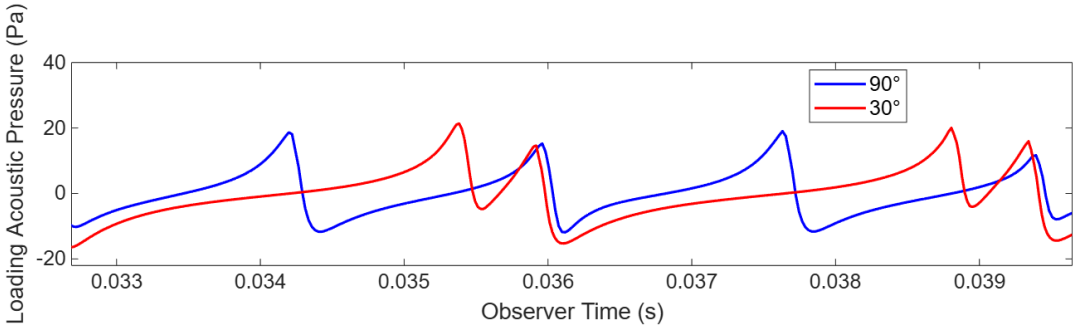

(b) $\Delta x = 0.5D$

Figure 4.10: Loading acoustic pressure comparison at 90° and 30° index angles.

The amplitude of the total acoustic pressure in the $\phi = 30°$ configurations aligns with that of the $\phi = 90°$ configuration for both stacking distances, as shown in Figures 4.11 and 4.12. All configurations demonstrate that the uneven blade spacing increases the number of tonal peaks, as seen in Figures 4.12a and 4.12b.

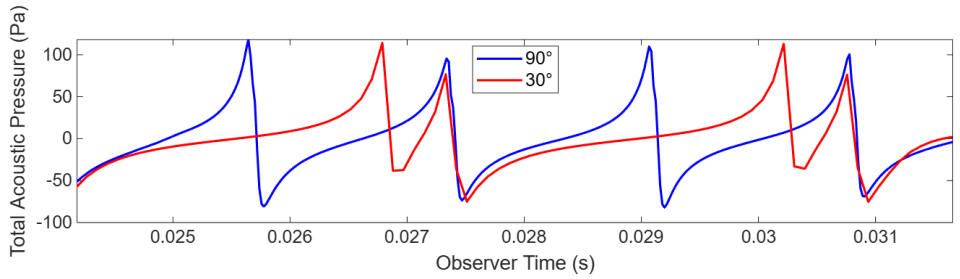

(a)

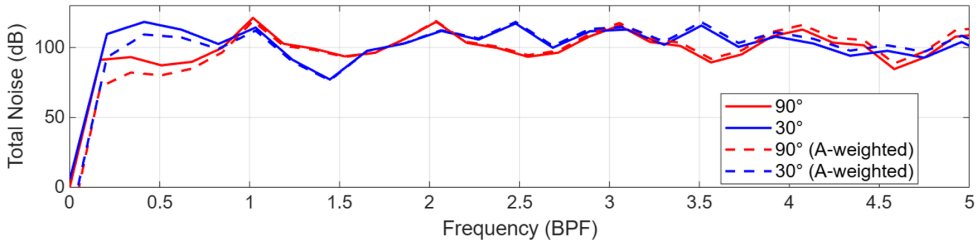

(b)

Figure 4.11: Total acoustic pressure (a) and total noise (b) comparison at 90° and 30° index angles ($\Delta x = 0.25D$).

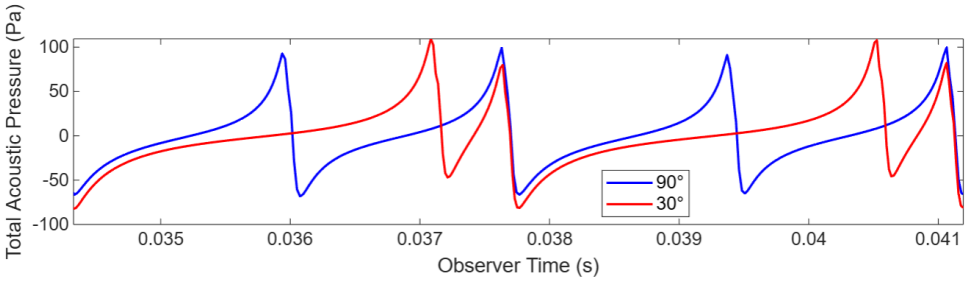

(a)

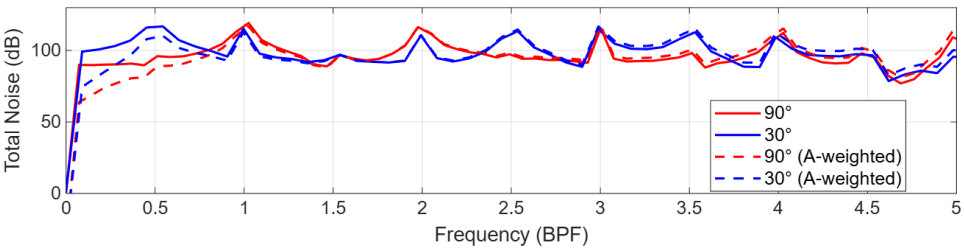

(b)

Figure 4.12: Total acoustic pressure (a) and total noise (b) comparison at 90° and 30° index angles ($\Delta x = 0.5D$).

4.3 5-Bladed Configurations

Additionally, two 5-bladed configurations were studied (Figure 4.14). The baseline configuration was an evenly spaced coplanar rotor. The second configuration consisted of the 3-bladed evenly spaced leading rotor and 2-bladed trailing rotor, separated by $0.25D$. This rotor setup created two $30°$, two $90°$ and one $120°$ angles between the adjacent blades. The simulations were conducted at an advance ratio of $J = 0.1$. The unevenly spaced configuration experienced a 2% thrust loss compared to the baseline case.

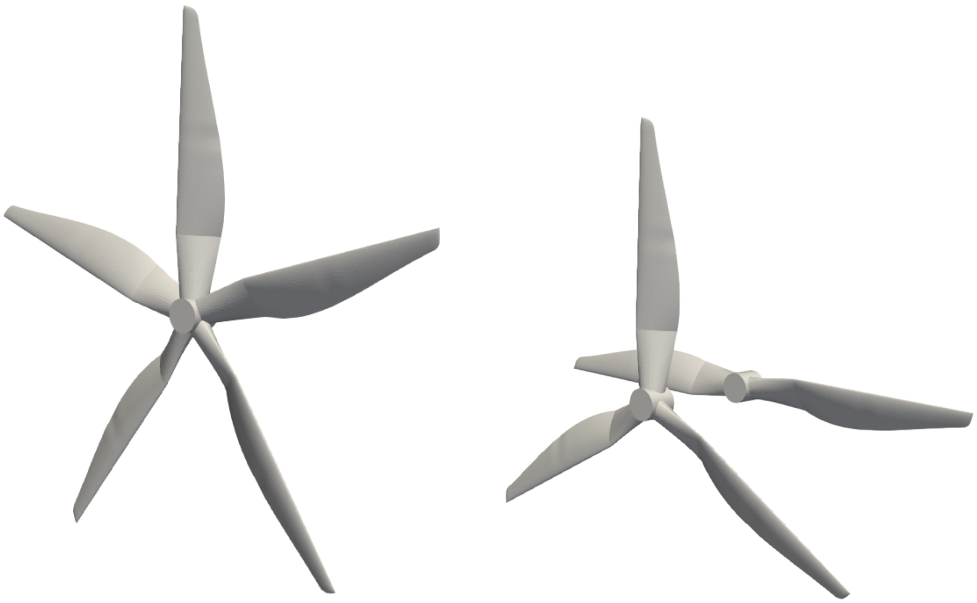

(a) Baseline configuration (b) $\phi_{min} = 30°$, $\Delta x = 0.25D$

Figure 4.13: 5-Bladed configuration

Figure 4.14 demonstrates the Q-criterion isosurfaces for the 5-bladed configurations. An interaction between the trailing blade and the wake that was created by the leading blade can be observed in Figure 4.14b.

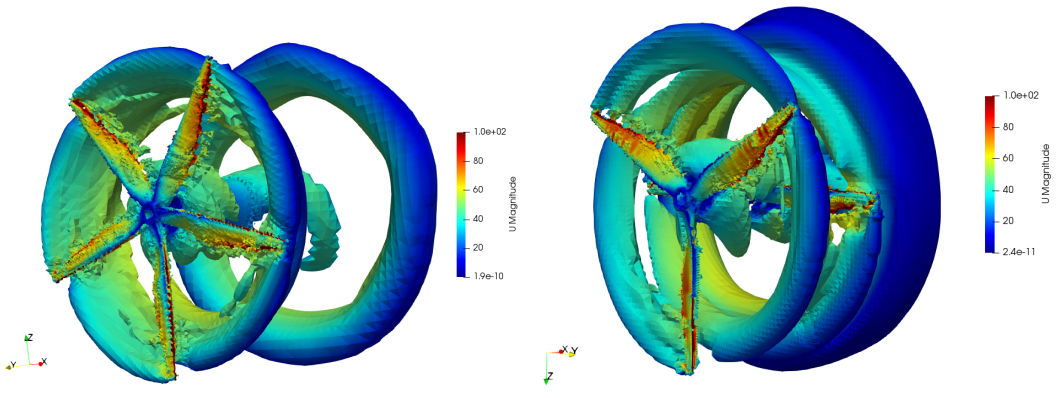

(a) Baseline configuration (b) $\phi_{min} = 30°$, $\Delta x = 0.25D$

Figure 4.14: Q-criterion, colored by the velocity.

As shown in Figure 4.16, the number of total acoustic pressure peaks corresponds to the number of blades. However, the spacing of the peaks differs significantly from the evenly spaced 5-bladed rotor, reflecting the azimuthal spacing between the blades.

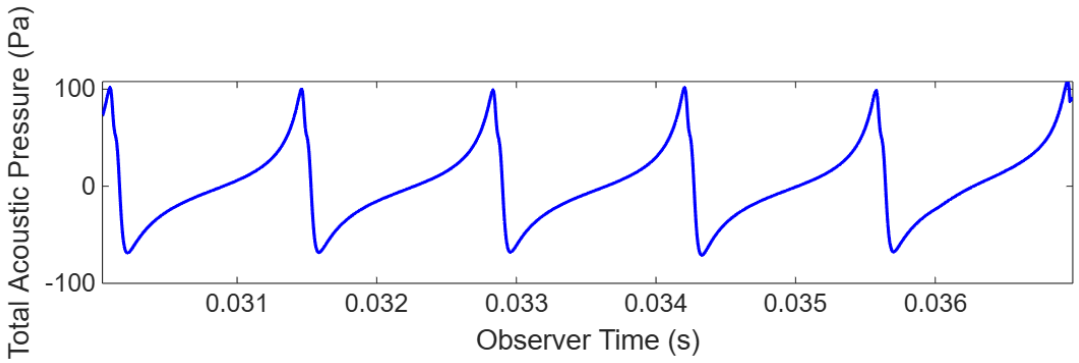

Figure 4.15: Baseline 5-bladed configuration.

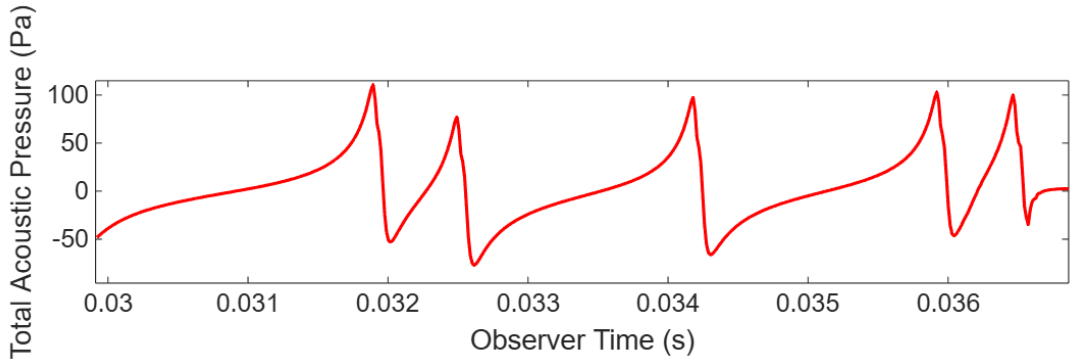

Figure 4.16: $\phi_{min} = 30°$, $\Delta x = 0.25D$ configuration.

BLANK

Chapter 5

Conclusions

5.1 Summary

The aeroacoustic and aerodynamic performance of rotors with uneven blade spacing was investigated numerically. The study was conducted using CFD simulations in the OpenFOAM software and aeroacoustic analysis in PSU-WOPWOP. The CFD simulations were carried out using uRANS as the governing equations, and sliding mesh approach to implement the rotation. Six stacked rotor configurations of the APC 27×13 propeller with two index angles ($\Delta\phi = 90°$, $\Delta\phi = 30°$) and three axial distances ($0D$, $0.25D$, $0.5D$) were investigated. The main conclusions of this work are:

1. **Steady-State comparison:** The results were compared against data obtained from MRF simulations of analogous rotor setups. The loading noise in the current study was significantly higher than in the MRF simulations. This discrepancy arises from the steady-state nature of the MRF approach, which does not capture the unsteady aerodynamic interactions between the fluid and the blades. This demonstrates the limitations of the MRF approach. However, the loading noise in both simulations is significantly smaller than the thickness noise, meaning it does not contribute greatly to the total noise produced by the rotors.

2. **Aerodynamic performance:** Configuration with ($\phi = 30°$, $\Delta x = 0.25D$) demonstrated the best aerodynamic performance among the tested cases. For $90°$ index angle, the configuration with $\Delta x = 0.25D$ was also the most efficient. Overall, the differences in thrust coefficients were relatively small, except for the coplanar case with $\phi = 30°$, that showed 6.46% thrust loss.

3. **The impact of uneven blade spacing:** Uneven blade spacing altered the periodicity of acoustic pressure peaks. While the $90°$ configurations produced four distinct and evenly spaced peaks, the $30°$ configurations generated only two main peaks, each followed by a smaller one. This resulted in the redistribution of tonal noise energy into lower frequency bands. The frequency spectra showed that uneven blade spacing introduced additional tones, spreading the noise energy over a broader frequency range. Additionally, the impact of the index angle remained significant in configurations with increased axial distance.

4. **The impact of axial distance:** Transient simulations allowed to capture the noise generated by unsteady aerodynamic phenomena, such as blade–vortex interaction. The results showed that loading noise decreased as the axial spacing between the rotors increased. This can be attributed to wake dissipation, which weakens the blade-vortex interactions and reduces their overall contribution to noise.

5.2 Recommendations for Future Work

To improve the accuracy of thrust predictions, future work should consider a rotor with better experimental data. The 25% difference between the experiment and simulation, highlights the importance of accurate inflow conditions, as the turbulent flow in the experimental setup can significantly influence the results.

To fully examine the effect of axial and angular modulation on the propeller efficiency, modulated configuration need to be studied over a wider range of advance ratios. The current study examined only one advance ratio ($J = 0.1$). However, the impact of axial and angular modulation on the aerodynamic performance may vary with changes in J. Investigating this dependency could provide more insights on the benefits of modulated configurations under different operation conditions.

Further investigation of the 5-bladed configurations under varying operating conditions is needed. The effect of angular modulation was observed in the acoustic pressure signal. However, additional testing of configurations with various index angles and axial distances is necessary to draw the conclusions about its effect on noise reduction.

Finally, future studies should include the directivity analysis of the emitted noise. To make conclusions about overall noise reduction, it is essential to investigate a grid of multiple observers placed in the plane of rotation. This would allow for a more full understanding of how modulation affects the distribution of sound.

Bibliography

[1] C. A. Network, "A review of 100 chinese low-altitude economy companies and 35 domestic evtol companies," 2025. Accessed: 2025-02-26.

[2] Joby Aviation, "Joby Aviation – Official Website," 2025. Accessed: 2025-04-03.

[3] Addcomposites, "evtol manufacturing: A deep dive into current trends and future opportunities," January 2025. Accessed: 2025-04-10.

[4] J. Paur, "Nasa's puffin: The one-man electric plane that vtols," 2010. Accessed: 2025-03-31.

[5] V. Mellert, U. Richter, H. Møller, L. Nielsen, K. Ashihara, and H. Takeshima, "Precise and Full-range Determination of Two-dimensional Equal Loudness Contours," Jan. 2003.

[6] X. Wang, "4 - Vehicle noise measurement and analysis," in *Vehicle Noise and Vibration Refinement* (X. Wang, ed.), pp. 68–92, Woodhead Publishing, Jan. 2010.

[7] M. Botre, K. Brentner, J. Horn, and D. Wachspress, *Validation of Helicopter Noise Prediction System with Flight Data*. May 2019.

[8] A. Vieira, *[MSc Thesis] Helicopter Rotor Noise: Development of an Acoustic Software Tool*. PhD thesis, Oct. 2013.

[9] T. Kim, "Reduction of tonal propeller noise by means of uneven blade spacing," master's thesis, University of California, Irvine, 2016. ProQuest ID: Kim_uci_0030M_13842, Merritt ID: ark:/13030/m5h46d2j.

[10] APC Propellers, "27x13e propeller," 2025. Accessed: 2025-04-01.

[11] C. Greenshields and H. Weller, *Notes on Computational Fluid Dynamics: General Principles*. Reading, UK: CFD Direct Ltd, 2022.

[12] J. B. Brandt, R. W. Deters, G. K. Ananda, O. D. Dantsker, and M. S. Selig, "Uiuc propeller database, vols 1-4," 2025. Accessed: 19.01.2025.

[13] C. Arystanbekov, A. Zhakatayev, and B. Elhadidi, "Passive rotor noise reduction through axial and angular blade spacing modulation," *Aerospace*, vol. 12, p. 167, 02 2025.

[14] L. Maxwell and G. Evans, "The effects of noise on pre-school children's pre-reading skills," *Journal of Environmental Psychology*, vol. 20, pp. 91–97, 03 2000.

[15] H. Wei, B. Lou, Z. Zhang, B. Liang, F.-Y. Wang, and C. Lv, "Autonomous navigation for evtol: Review and future perspectives," *IEEE Transactions on Intelligent Vehicles*, vol. 9, no. 2, pp. 4145–4171, 2024.

[16] R. C. Mellin and G. Sovran, "Controlling the tonal characteristics of the aerodynamic noise generated by fan rotors," *Journal of Basic Engineering*, vol. 92, pp. 143–154, 03 1970.

[17] H. Fletcher and W. A. Munson, "Loudness, Its Definition, Measurement and Calculation," *The Journal of the Acoustical Society of America*, vol. 5, pp. 82–108, Oct. 1933.

[18] M. J. Lighthill, "On sound generated aerodynamically I. General theory," *Proceedings of the Royal Society of London. Series A. Mathematical and Physical Sciences*, Mar. 1952. Publisher: The Royal SocietyLondon.

[19] J. E. Ffowcs Williams and D. L. Hawkings, "Sound Generation by Turbulence and Surfaces in Arbitrary Motion," *Philosophical Transactions of the Royal Society of London Series A*, vol. 264, pp. 321–342, May 1969.

[20] W. Dobrzynski, "Propeller Noise Reduction by Means of Unsymmetrical Blade-spacing," *Journal of Sound and Vibration*, vol. 163, pp. 123–126, May 1993.

[21] C. E. Tinney and J. Valdez, "Thrust and Acoustic Performance of Small-Scale, Coaxial, Corotating Rotors in Hover," *AIAA Journal*, vol. 58, no. 4, pp. 1657–1667, 2020. Publisher: American Institute of Aeronautics and Astronautics _eprint: https://doi.org/10.2514/1.J058489.

[22] S. Whiteside, N. Zawodny, X. Fei, N. A. Pettingill, M. D. Patterson, and P. Rothhaar, "An Exploration of the Performance and Acoustic Characteristics of UAV-Scale Stacked Rotor Configurations," in *AIAA Scitech 2019 Forum*, American Institute of Aeronautics and Astronautics. _eprint: https://arc.aiaa.org/doi/pdf/10.2514/6.2019-1071.

[23] Y. Hong, D. Lee, S. Yang, H. Kook, and K. Yee, "Exploration of stacked rotor designs for aerodynamics in hover," *Aerospace Science and Technology*, vol. 141, p. 108557, Oct. 2023.

[24] S. Platzer, M. Hajek, P. Mortimer, J. Sirohi, and J. Rauleder, "Investigation of the Flow Fields of Coaxial Co-Rotating and Counter-Rotating Rotors in Hover Using

Measurements and Simulations," *Journal of the American Helicopter Society*, vol. 68, Oct. 2023.

[25] E. Grande, S. Shubham, F. Avallone, D. Ragni, and D. Casalino, "Computational aeroacoustic study of co-rotating rotors in hover," *Aerospace Science and Technology*, vol. 153, p. 109381, Oct. 2024.

[26] D. C. Wilcox, "Formulation of the k-w turbulence model revisited," *AIAA Journal*, vol. 46, no. 11, pp. 2823–2838, 2008.

[27] D. C. Wilcox, *Turbulence Modeling for CFD*. DCW Industries, Inc., 2nd ed., 2004.

[28] S. V. Patankar and D. B. Spalding, "A calculation procedure for heat, mass and momentum transfer in three-dimensional parabolic flows," *International Journal of Heat and Mass Transfer*, vol. 15, pp. 1787–1806, 1972.

[29] F. Farassat and G. P. Succi, "The prediction of helicopter rotor discrete frequency noise," in *In: American Helicopter Society*, pp. 497–507, Jan. 1982.